

UMTRI
96412

TWENTY-FOUR-MONTH REPORT

ON

CONTRACT PH-43-67-1136

by

J. W. Melvin, Project Engineer

V. L. Roberts, Project Director

Highway Safety Research Institute
The University of Michigan
Ann Arbor

Transportation
Research Institute

UMTRI
96412

ACKNOWLEDGMENTS

The authors of this report wish to acknowledge the assistance of the following persons in carrying out the research outlined in this progress report and its preparation: G. Bahling, S. Fisher, P. Fuller, W. Hall, J. Morgan, W. Olmsted, C. Shinn, C. Snow, S. Stewart, P. Van Luven, C. Weston, and J. Warden of the Biosciences Division of the Highway Safety Research Institute; B. H. Karnopp of the Department of Engineering Mechanics at The University of Michigan; D. F. Huelke, Professor, and F. G. Evans, Professor of the Department of Anatomy of The University of Michigan; and P. W. Gikas, Chief of Clinical Laboratory Services at the Veterans Administration Hospital in Ann Arbor, Michigan and R. C. Hendrix, Professor of Pathology at The University of Michigan whose assistance is proving most valuable in obtaining tissues at autopsy.

Transportation
Research Institute

TABLE OF CONTENTS

I. INTRODUCTION	1
II. EXPERIMENTAL PROGRAM	4
A. Hard Tissue Tests	4
1. Skull Bone Radial Compression Tests	4
2. Mechanical Response of Human Cranial Compact Bone in Tension	16
3. Shear Tests	25
4. Composite Structural Testing of Skull Bone	27
B. Brain Tissue Tests	30
C. Other Soft Tissue Tests	46
1. Dura Mater Tests	46
2. Scalp Tests	49
III. ANALYTICAL PROGRAM	57
APPENDIX A. A Mathematical Model to Determine Viscoelastic Behavior of In Vivo Primate Brain.	

I. INTRODUCTION

The nature of this twenty-four month interim report to the Head Injury Model Committee is quite different from the previous reports. In the past, the emphasis has been on experimental technique, test development and raw data display. This report deals mainly with the first steps towards finalizing the various mechanical properties of the tissues of the head in the form of statistically summarized stress-strain curves and physical constants. From these summary curves it has been possible in some cases to indicate promising classes of candidate synthetic materials. In other cases more work is necessary to reach this level.

It is evident from the results to date that statistic analysis alone is not sufficient to determine the mechanical properties of the tissues of the head in a meaningful manner that will provide a rational course for synthetic head model design. Statistics must be guided by the findings of functional histology, materials science and theoretical analysis in order to achieve the goals of the project in the most effective manner. Such studies have been a continuing part of our program throughout the past two years. A typical example of this combined approach is found in the in vivo primate brain property studies. In order to fully understand the mechanics of the dynamic probe and monkey brain as a total system, a completely theoretical analysis of the system was performed (see Appendix A of this report). In a parallel manner continued work on the experimental data has led to special techniques for reduction of the data. These two separate approaches are now being combined in order to facilitate our understanding of this very important phase of the project.

Another example of the combined approach to the understanding of material properties is in our work with skull bone. There is an increasing amount of

data being accumulated to substantiate Dr. McElhaney's hypothesis that the large variations in the skull bone tests are due to structural differences rather than material differences. A porous block model for skull bone which consists of a bone matrix with uniform properties and varying void content has been developed. The behavior of this model characterizes our observations on skull bone both as to the observed anisotropy and the strong density dependence of mechanical properties. We are currently developing this model to show that the mechanical behavior of skull bone can be duplicated by a single component material with a suitably dispersed void content.

Additional substantiation of the strong dependence of the mechanical properties of bone on its macrostructure is contained in our continuing histological studies of the fracture sites of tension specimens. Low strength tests generally show the fracture initiated at a source of stress concentration while high strength tests generally involve a fracture surface with little or no macro-discontinuities.

Consideration of the envelope of the tensile stress-strain curves of skull bone (Figure 10) shows that other types of bone also fit in this range. (See for example "Stress and Strain in Bones" by F. Gaynor Evans, C. C. Thomas, 1957). The tensile modulus of compact bone for the human femur averages 2×10^6 psi while cancellous bone from the human vertebrae averages 2.5×10^3 psi. The density of the femur bone is only slightly higher than the most dense skull bone.

The goal of phase one of the Head Injury Model Construction Program is the specification and characterization of those physical properties of the tissues of the head relevant to head injury and necessary to select suitable substitute materials. Under the guidance of the H.I.M.C. Committee we have concentrated our efforts on the properties of the skull, scalp, dura and brain.

The experimental program on skull bone properties is nearing completion. The important physical properties have been measured on a large number of specimens and statistical analysis of the data is practically complete. A variety of regression analysis is being developed as well as a summary characteristic model. A limited number of tests on promising substitute candidate materials is planned.

The experimental program on scalp still requires a significant effort for completion. An adequate source of human material has been established. Some compression testing at various rates has been done and a sufficient number of these will be performed in the current contract year to allow a meaningful statistical analysis. Tensile testing is still under development and requires special gripping methods because of the subcutaneous fatty layer prominent in the human. Hopefully, this problem will be overcome and significant tensile testing accomplished.

The dura tensile test program is well under way and should be completed by the end of this contract year. A coupling of the histological study with the tensile test data shows promise of isolating observed anisotropies.

The test program on the mechanical properties of brain tissue has been developed to the point that some correlation of in vivo and in vitro bulk properties can be made. The techniques and information developed during the past two years will be applied in the present contract year to studying regional variations in human brain. High strain rate compression tests of human brain will also be performed as an additional study in the characterization of brain properties. Preliminary testing of promising substitute candidate materials will also be incorporated into the test program.

II. EXPERIMENTAL PROGRAM

A. Hard Tissue Tests

1. Skull Bone Radial Compression Tests. (J. W. Melvin and I. Barodawala)

All of the compression testing of skull bone in the Biomaterials Laboratory has been performed on human skull bone tested in the radial direction. The majority of the tests have been on specimens consisting of the diploë layer of unembalmed human skull obtained at autopsy and stored at -10°C until used. Some tests have been performed on specimens which included inner and outer table material as well as diploë. Specimens of this type were also used in the special whole calvarium compression tests of embalmed bone which were reported in Special Report No. 1, 23 May 1969.

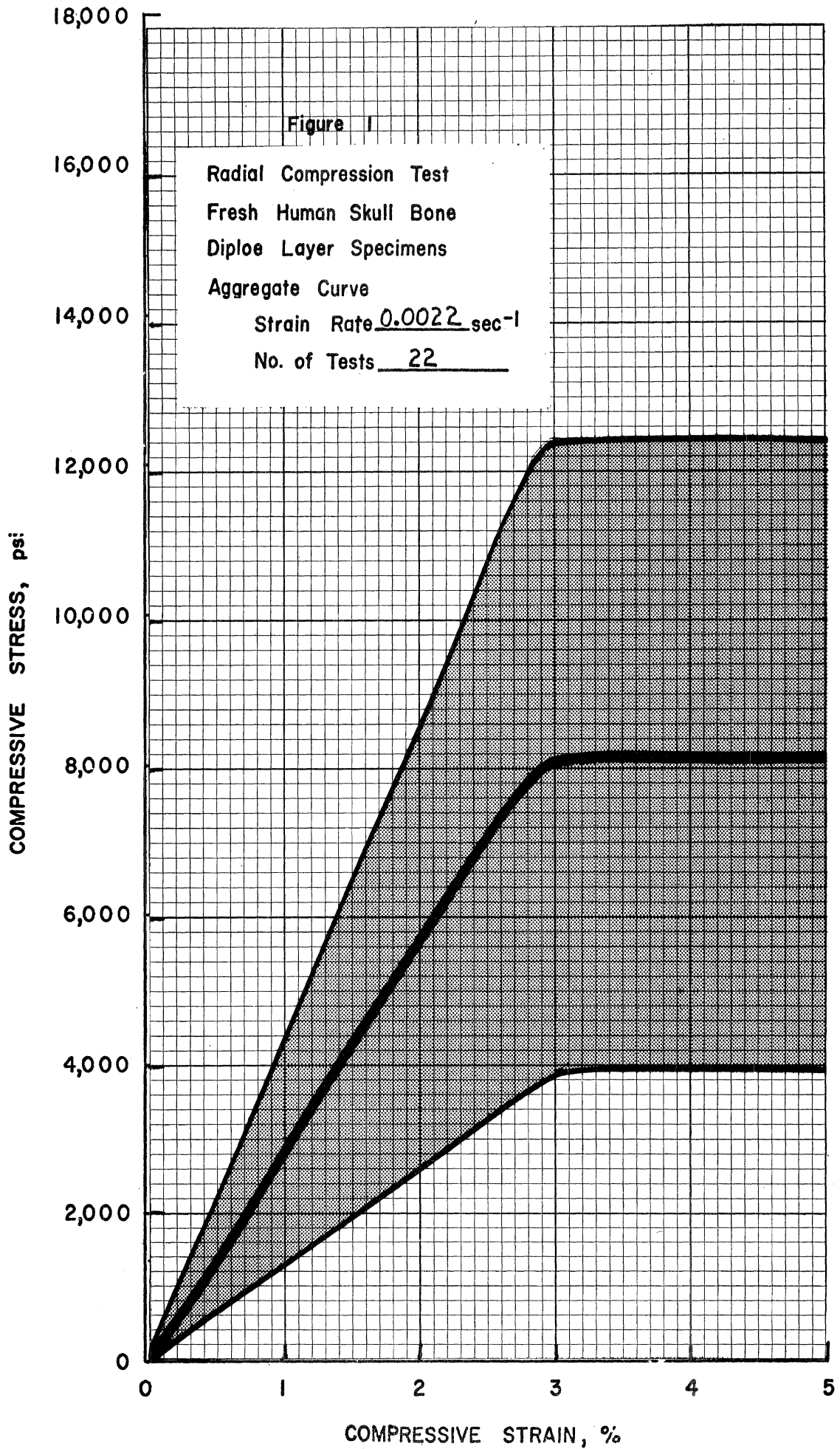
The specimens consisting of diploë only are the most useful type of specimen for characterizing the mechanical properties of the diploë layer as a material. The other types of specimens are actually two phase structures and must be analyzed as such. All basic compression testing at strain rates up to in excess of 500 sec^{-1} has been completed in the past six months.

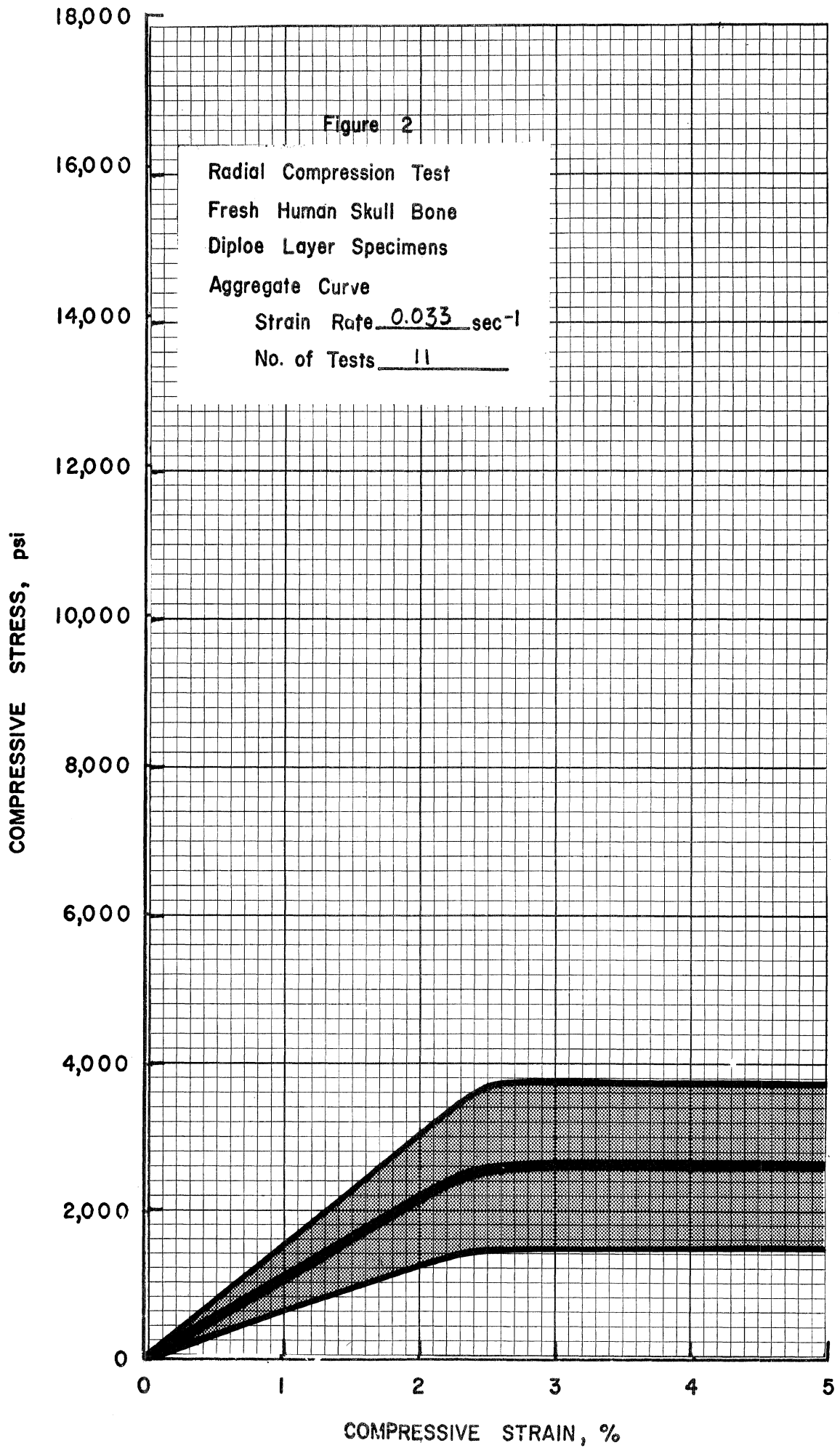
The techniques and procedures used in this work have been reported in previous interim reports. The specimens were all diploë only. A summary of the data at each of the nine strain rates used is given in Table I. An alternate, graphical form of representing the same data is shown in Figures 1-9. Here the mean compressive stress-strain curve is constructed from Table I information. Also, the bounds of one standard deviation on either side of the mean curve is shown. Since the majority of the test data exhibited the zero slope collapse type of compressive failure the curves were drawn accordingly. Taken at face value, the data exhibits the wide variation typical of diploë layer data. The key to

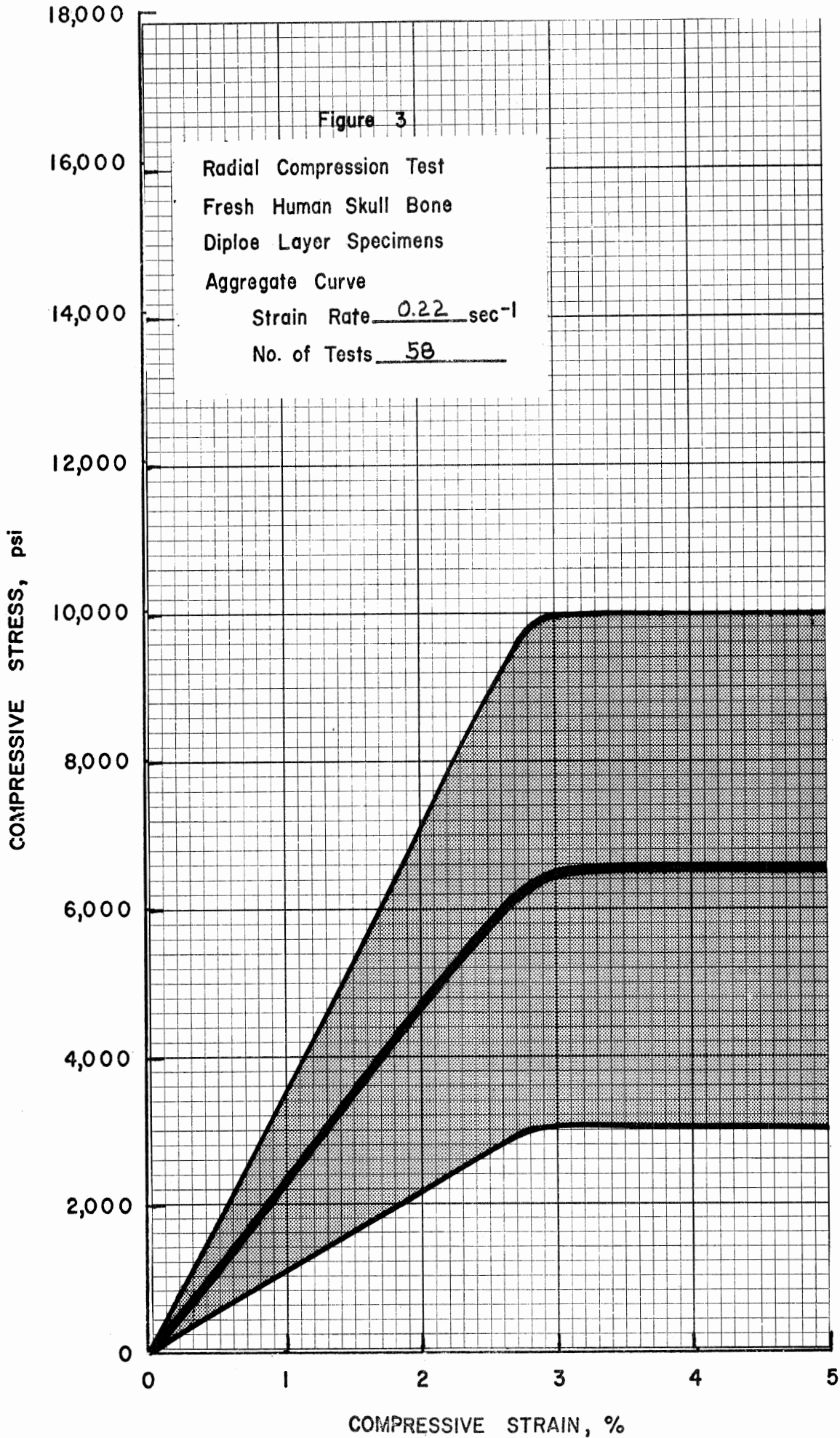
understanding this variation was shown in the eighteen-month report to be the relationship between compressive strength σ_c , compressive modulus E_c and specimen specific weight γ . Statistical analysis of this data with the goal of determining $\sigma_c = f_1(E_c)$, $\sigma_c = f_2(\gamma)$ and $E_c = f_2(\gamma)$ relationships is presently being carried out. Preliminary results indicate multiple correlation coefficients for some trail relations in the range from 0.85 to 0.97. Once these relations have been developed and verified at each strain rate we will have an effective means of determining strain rate effects which are now masked by specific weight variations. These relationships between properties and specific weight are also going to be used in conjunction with models of two phase structures to analyze the composite type compression test specimens. The analytical results will then be compared with the composite specimen test data for confirmation of the analysis.

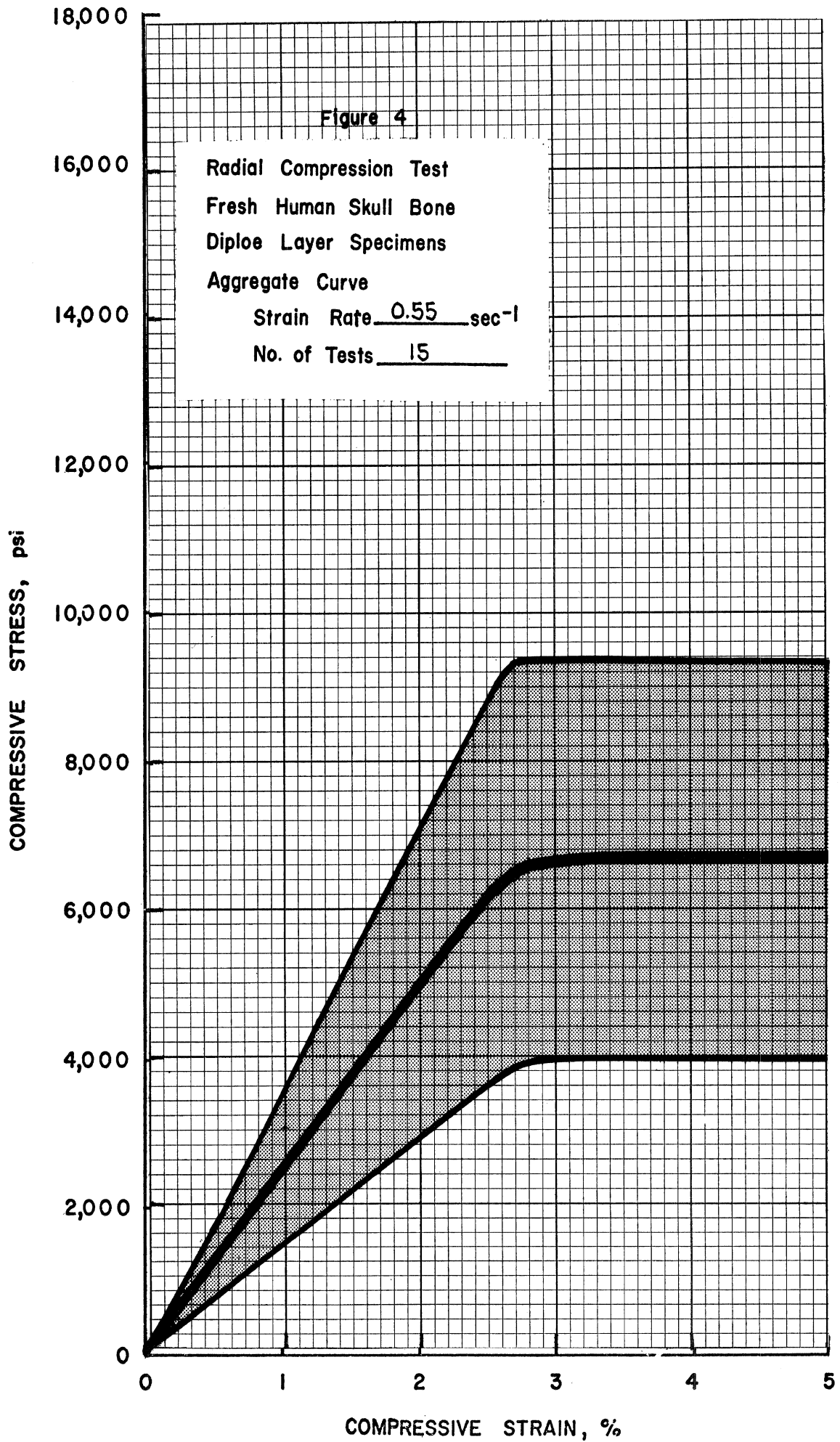
TABLE I. SUMMARY OF RADIAL COMPRESSION TESTING

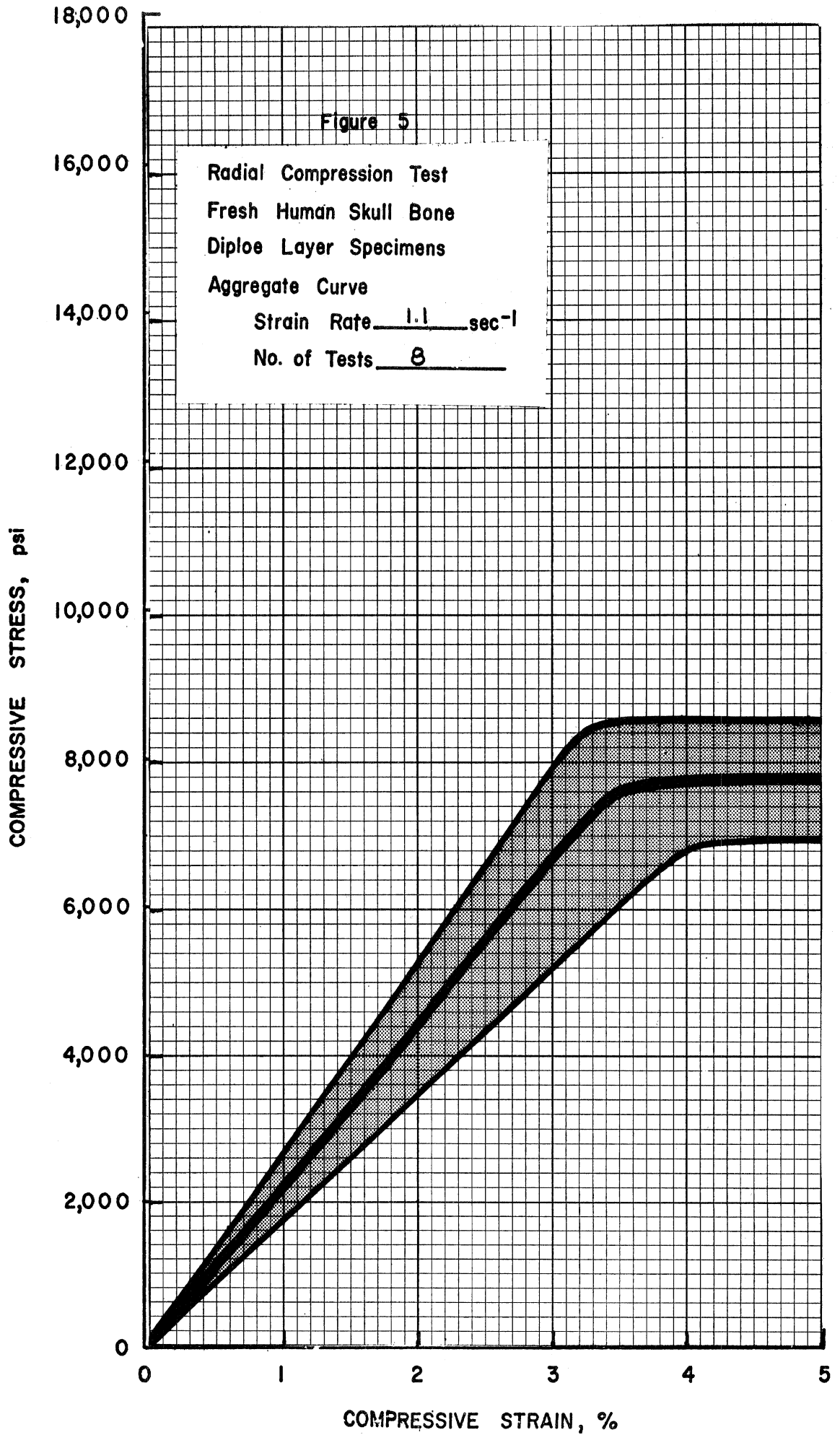
Strain Rate sec ⁻¹	Mean σ_c psi	Mean E_c 10 ⁵ psi	Mean γ lbs/in ³	St. Dev. σ_c psi	St. Dev. E_c 10 ⁵ psi	St. Dev. γ lbs/in ³	Total No. of Specimens	Total No. of Persons
0.0022	8,172	2.826	0.0517	4,242	1.506	0.0108	22	3
0.033	2,596	1.081	0.0384	1,126	0.443	0.00495	11	2
0.22	6,532	2.314	0.0493	3,529	1.313	0.0120	58	11
0.55	6,652	2.511	0.0511	2,734	1.040	0.0101	15	3
1.1	7,704	2.216	0.0438	855	0.428	0.00992	8	2
2.2	7,604	2.440	0.0483	5,569	1.519	0.0105	70	14
22.2	3,298	1.026	0.0415	809	0.349	0.00302	7	1
222	11,832	3.028	0.0492	8,980	2.226	0.00827	46	10
555	10,862	3.401	0.0509	7,328	2.199	0.00727	40	7

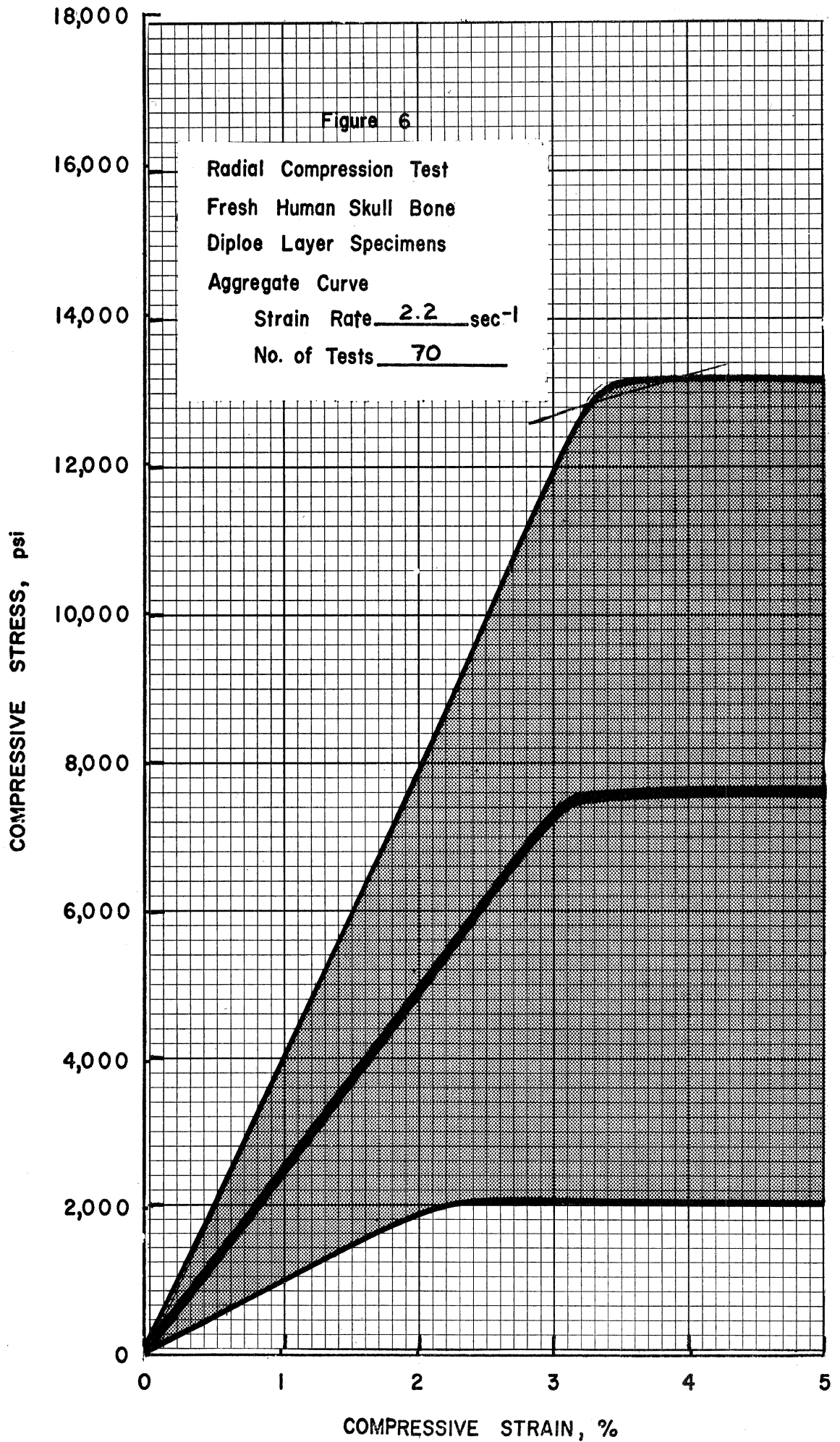


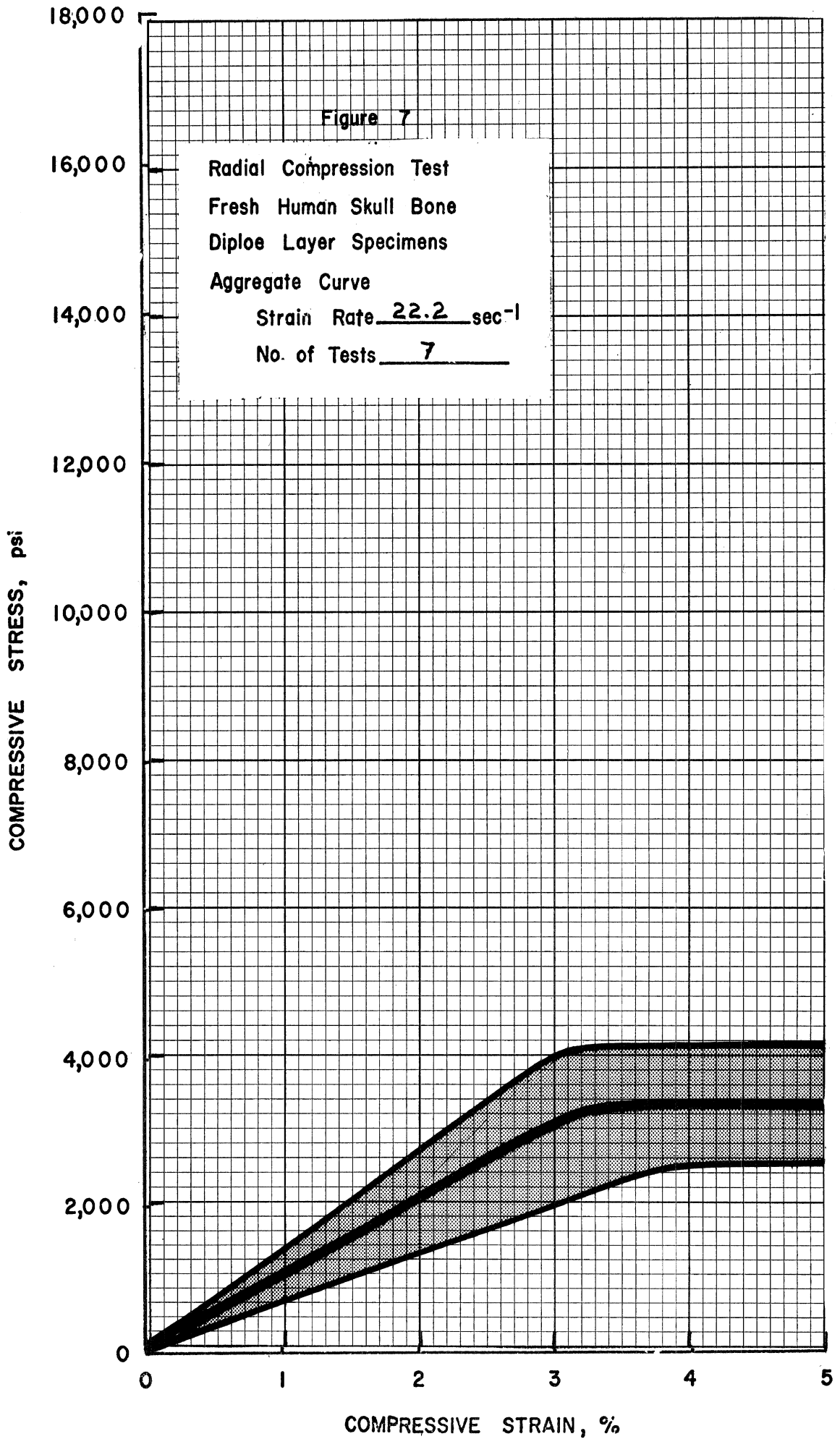


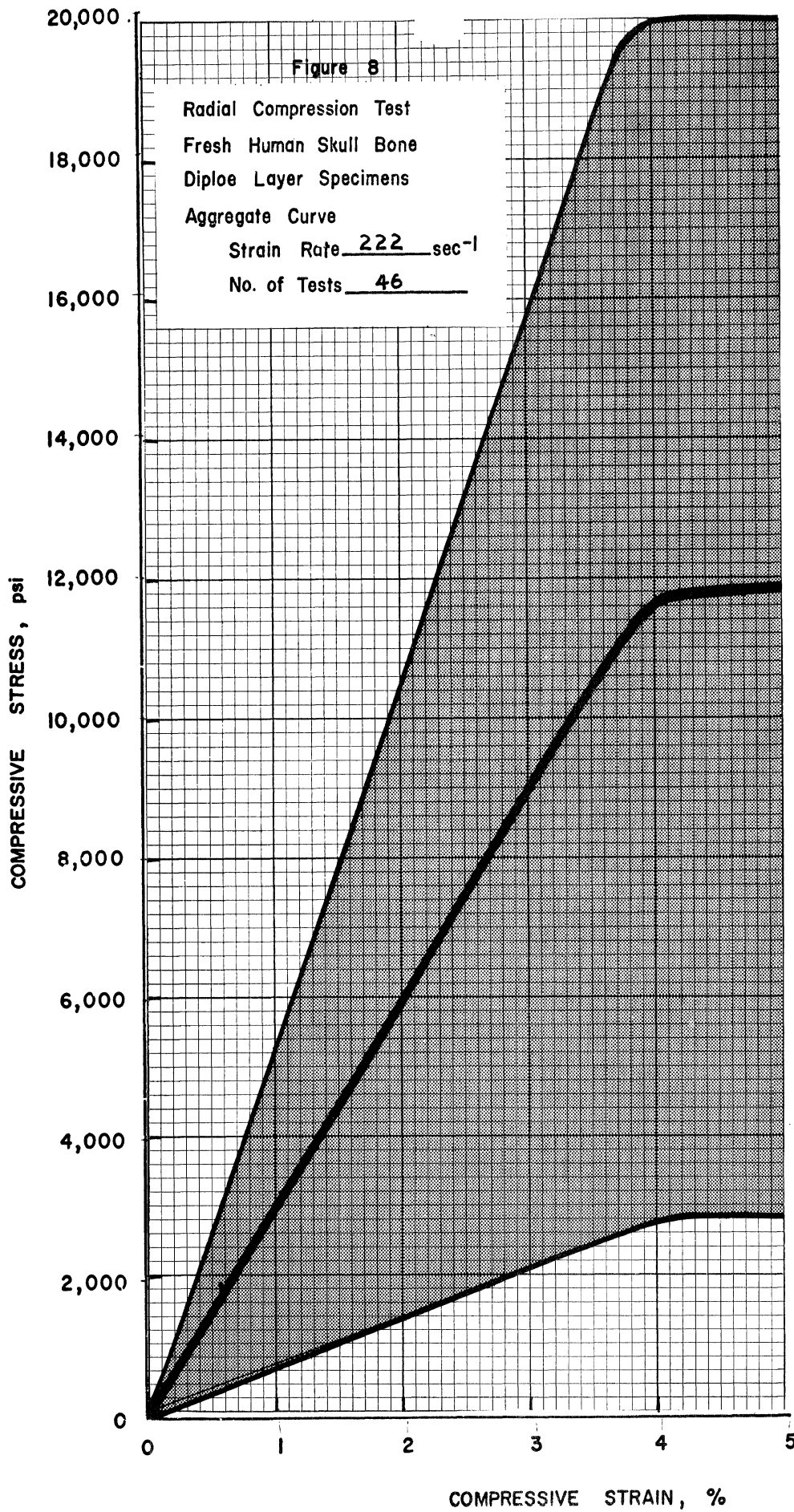


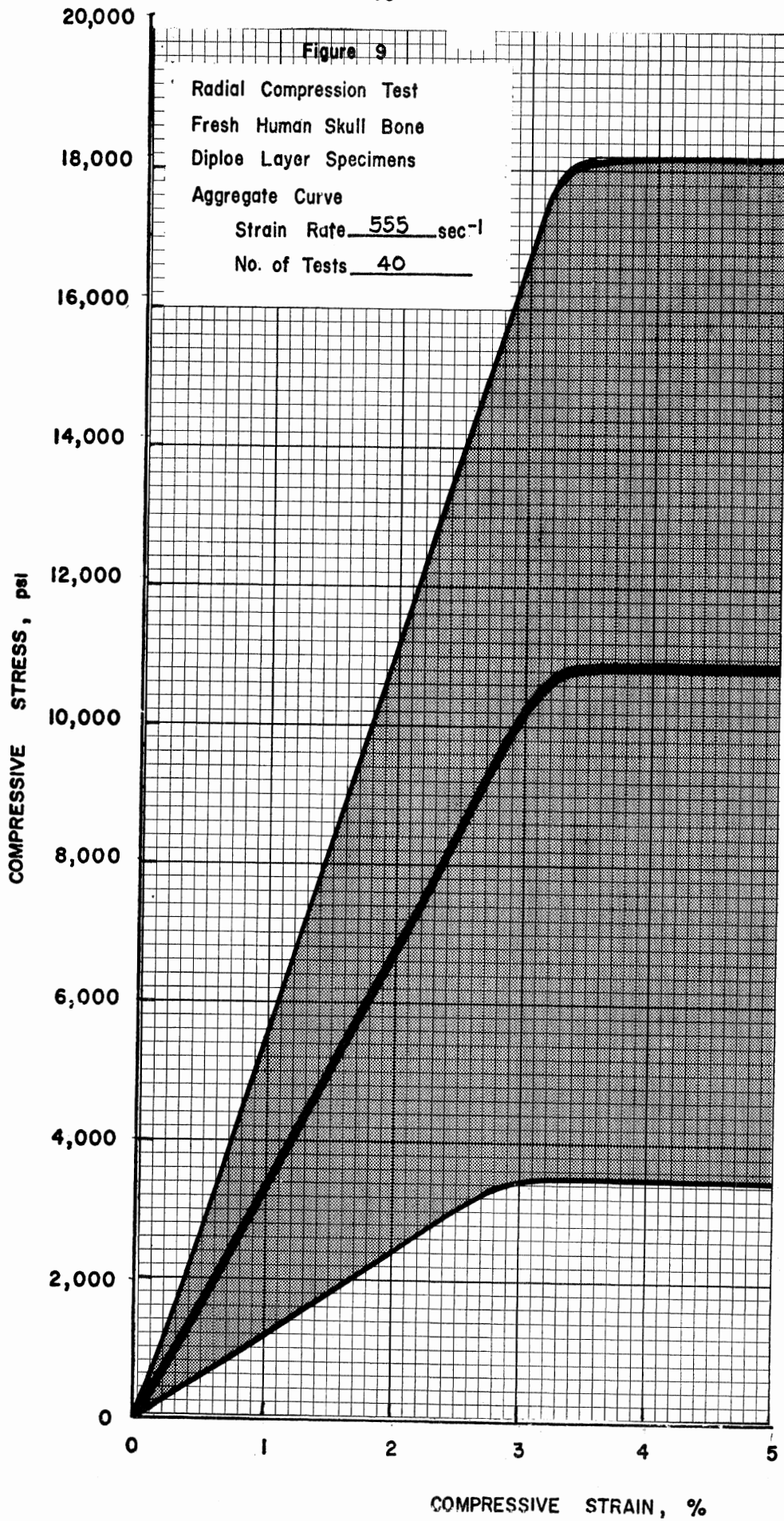












2. Mechanical Response of Human Cranial Compact Bone in Tension. (J. L. Wood)

The collection of tensile data has been completed and the immediately available results are included in the following paragraphs. Some data require statistical analyses which is currently under way. This report contains an outline of the entire program and details both the experiments that were performed as well as data analysis that will be completed by the end of August and will be forwarded to NIH in a special report.

a. Description of problem and significance of investigation.

Although the literature on mechanical properties of bone is extensive, it contains only two papers dealing with properties of cranial bone. Since cranial bones consist of outer and inner tables of compact bone, the properties of compact bone from other parts of the body might be used as an approximation. Most of the available data, however, is for long bones which are known to be anisotropic. Dempster's split line studies of the skull indicate that cranial bone might be isotropic in directions tangent to the surface of the skull, thus, there is a need to know something about the directional properties of cranial bone.

Penetration studies of the skull performed at The University of Michigan for the Ford Motor Company have shown strain rates as high as 30 in/in/sec resulting from impacts at 30 miles per hour. Hence, there is a need to investigate the effect of strain rate on the properties of cranial bone. McElhaney has investigated the properties of specimens from beef and embalmed human femur in compression at high strain rates, but there is no tensile data on strain rate properties of human bone.

b. Objectives of investigation.

The investigation was carried out to determine the mechanical characteristics of the compact layers of human cranial bones in sufficient detail to

select a material with similar behavior for a physical head model and to enable analytical analysis of head models to proceed.

- (1) Experimentally determine tensile stress-strain curves for cranial bones with respect to:
 - (a) Type of bone (parietal, temporal, frontal).
 - (b) Variation within an individual.
 - (c) Directional variation.
 - (d) Population variation.
 - (e) Strain rate.
 - (2) Statistically analyze the data.
 - (3) Attempt to deduce a functional relationship between stress, strain and strain rate.
- c. Experiments performed.
- (1) Selection of specimens - specimen size.
 - (a) Parietal bone - outer table.
 - (b) Frontal bone - outer table.
 - (c) Temporal bone - outer table.
 - (d) Inner table.
 - (2) Specimen preparation.
 - (a) Machining.
 - (b) Strain gaging.
 - (3) Static tests.
 - (a) Crosshead rates of 0.02 to 20 in/min - corresponding to strain rates of 0.0003 to 0.3 sec⁻¹.
 - (b) Grips.

(4) Dynamic tests.

(a) Crosshead rates of 200 to 10,000 in/min - corresponding to strain rates of 3.0 to 150 sec^{-1} .

(b) Grips.

(c) Load measuring system.

(d) Strain measuring system.

(e) Triggering system.

(5) Calibration and dynamic response of load and strain measuring systems.

(6) Data recording.

d. Data analysis.

(1) Comparison of properties within a bone plug from a single individual.

(a) All specimens from a given direction.

(b) Specimens from perpendicular directions.

(c) Specimens at different strain rates.

(2) Comparison of properties from several individuals.

(a) All specimens at a given strain rate - average curve.

(b) Average curves at different strain rates.

(c) Average curves for different bones (parietal, frontal, etc.).

(3) Effects of strain rate.

(a) Ultimate strength.

(b) Ultimate strain.

(c) Young's modulus.

(d) Energy absorbed.

(4) Curve fitting to arrive at a constitutive equation.

e. Equipment list.

(1) Specimen manufacture and preparation.

(a) Unimat lathe - milling machine.

(b) Strain gages and supplies.

- (2) Specimen testing.
 - (a) Grips and adaptors.
 - (b) Test machines.
 - (b.1) Instron.
 - (b.2) Plas-tech high speed machine.
 - (c) Load cells.
 - (c.1) Instron 50 pound strain gaged load cell.
 - (c.2) Kistler 1,000 pound crystal load cell.
 - (d) Strain gage bridge and DC amplifier.
 - (e) Data recording.
 - (e.1) Tektronix model 547 oscilloscope.
 - (e.2) Polaroid camera and film.

Over 300 specimens were machined in the course of this investigation. Many were rejected as unfit for testing because they included part of the diploë in their thickness. Others of these small, delicate specimens broke before they could be tested or were broken in the development of gripping and recording techniques. One hundred and thirty good stress-strain curves were obtained, representing data from 30 people, aged 25 to 95 years. Table II summarizes the number of bone plugs used from each area of the skull and in parenthesis the total number of good tests obtained from each area. Eight specimens of diploë in tension from 3 different plugs and 6 specimens having a suture running through the test section also were tested.

The following observations can be made about the compact bone of the inner and outer tables of the skull.

- (1) Specimens from perpendicular directions within a single bone plug do not have distinguishably different stress-strain curves. That is, in the tangential phase skull bone is approximately isotropic.
- (2) There is more variation between people than within a single person.
- (3) The modulus of this bone in tension is rate sensitive. An analysis is currently being done on strength, deformation and energy as a function of rate.
- (4) Freezer storage at -10°C does not seem to affect the properties of cranial bones.
- (5) Sutures tested in tension have very little strength. Future experiments investigating the bending strength of a beam cut from the braincase, with and without a suture, are planned.

Figure 10 gives a summary of the data from all tests performed, including all ages, types of bone and strain rates. The two lines originating from (0,0) give the limits of modulus encountered: 1.5×10^6 to 3.2×10^6 lb/in². The polygon encloses all of the failure points. This type of representation will be helpful in selecting candidate materials for the synthetic skull model. Obviously, the stress-strain curve of any candidate material should fall within this region. As an example, Figure II shows the envelope of Figure 10 with an overlay of the data envelope of a typical polyester plastic with glass fiber reinforcement. This material can certainly be classified as a preliminary candidate material. On the other hand, the stress-strain curve for Lexan, which was tested in May

for the HIM committee, is shown in Figure II for comparison. Even though the ultimate strength of Lexan would seem to qualify it as a candidate material, it does not match the envelope of skull bone very well at all. Once synthetic materials have been culled by the envelope technique, the next step will be the adjustment and refinement of the most promising synthetic materials in order to match the results of the statistical analysis of this tension test data.

TABLE II SUMMARY OF TENSION TESTS

The locations of specimens and numbers of tests performed on each type of bone.

	PL	PR	FL	FR	TL	TR
OT	12(53)	9(35)	3(9)	2(8)	1(6)	1(2)
IT	1(5)	-----	3(9)	1(2)	1(1)	-----

PL = parietal left

TL = temporal left

PR = parietal right

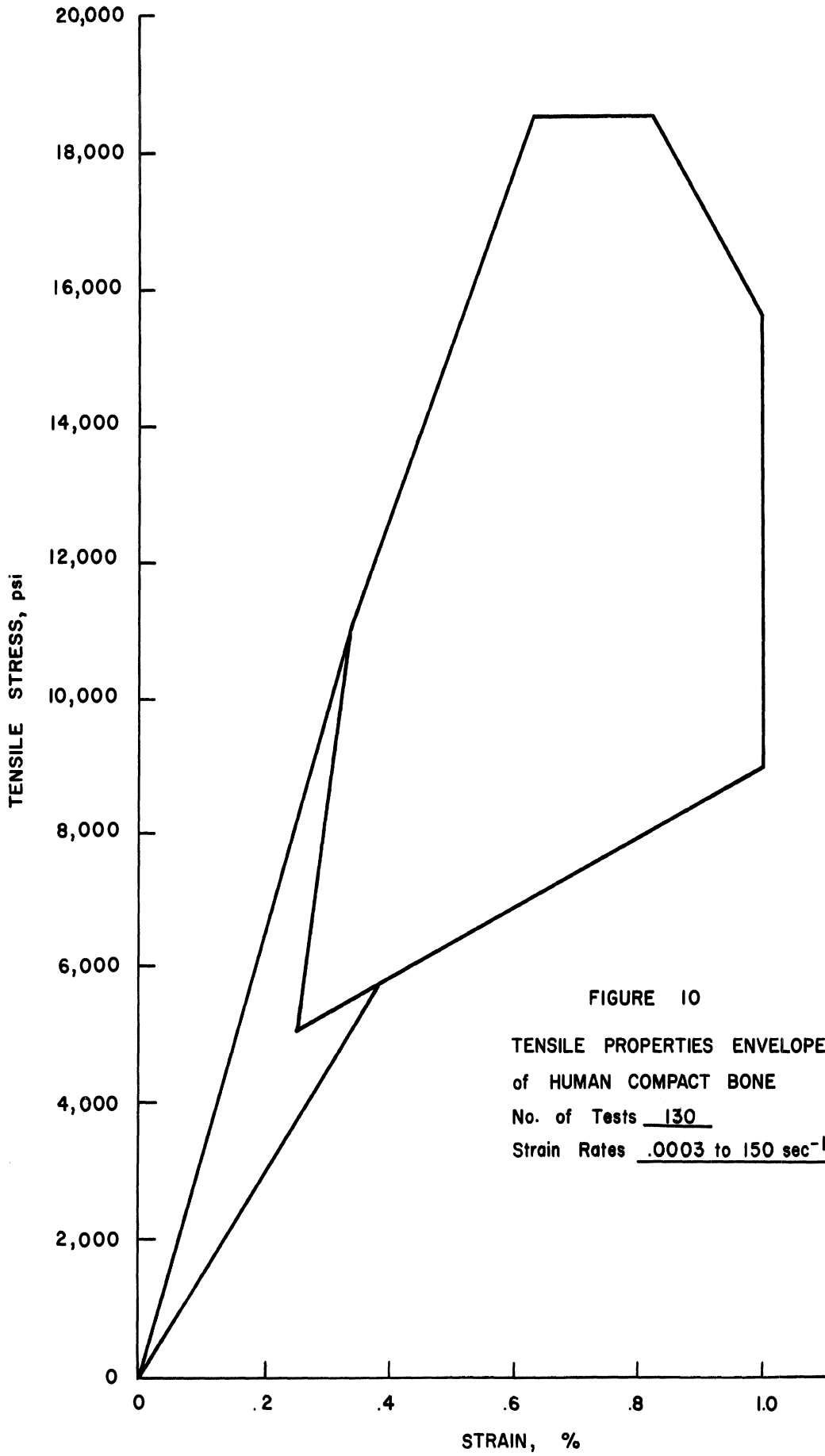
TR = temporal right

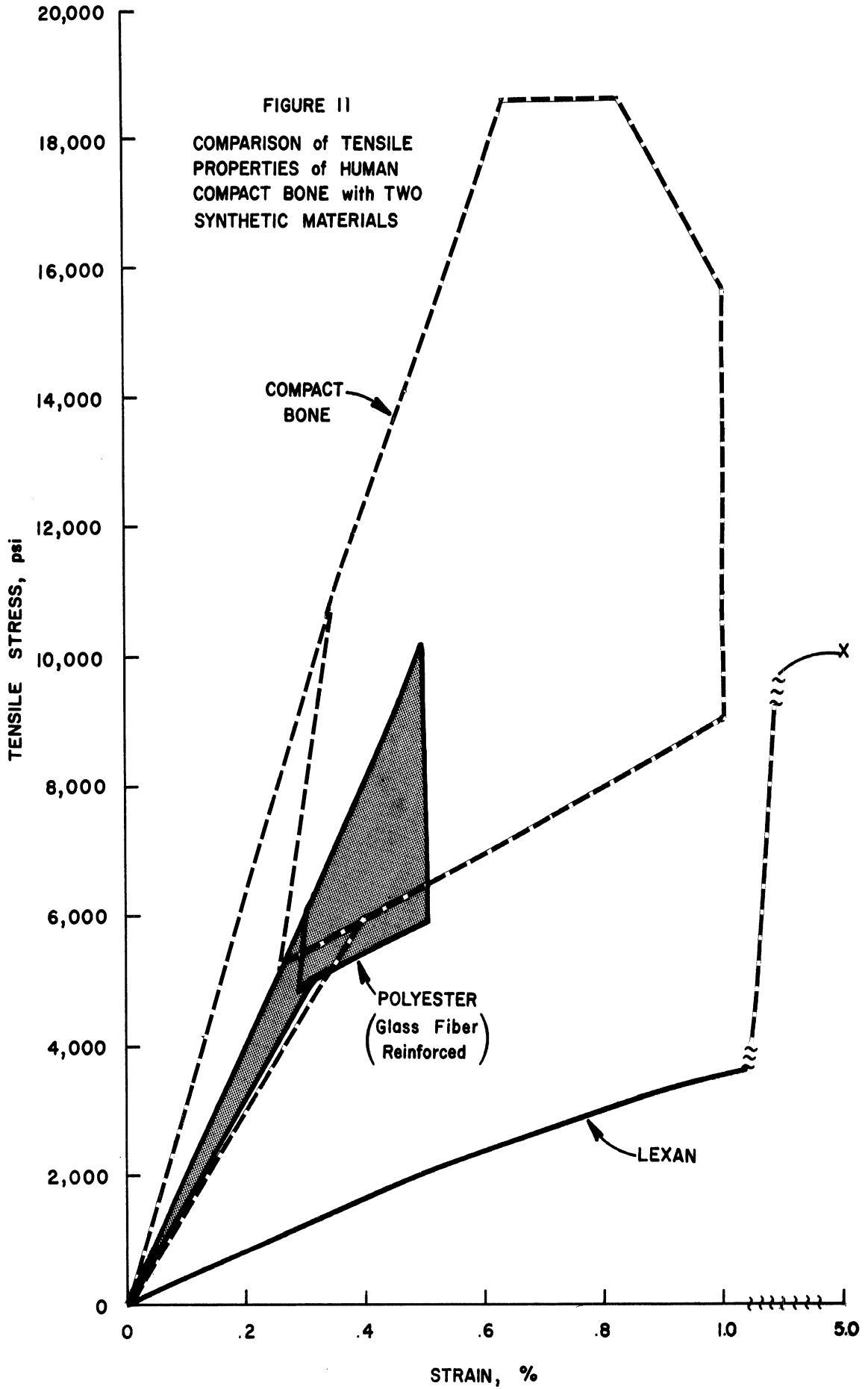
FL = frontal left

OT = outer table

FR = frontal right

IT = inner table





3. Shear Tests.

Large numbers of direct shear tests on the diploë layer of embalmed calvaria have been reported in all three of the previous interim reports. The main finding from these tests has been the highly variable nature of the shear strength of the diploë layer. This variation can be attributed mainly to person to person variation and position variation on the surface of the skull (twelve-month report). In view of the success of correlating the compressive properties of the diploë layer with diploë specific weight it was felt that the same may be done for the shear tests. In other words, the large variations in the shear tests may also be a direct consequence of diploë layer specific weight variations. Furthermore, examination of the mode of failure exhibited by the compression specimen shown in Figure 12, where the loading was in the vertical direction of the picture, suggests the possibility that the same mode of failure (splitting of the trabeculae) might occur if the specimen were loaded in transverse shear. Thus, the failure mechanism in shear may be quite similar to that in compression. The rough averages of typical diploë shear strengths are about one half the average diploë compressive strengths which would follow if the failure processes were similar.

In order to investigate the above hypothesis a series of combined experiments is now under way. Using both fresh and embalmed material, shear specimens will be taken in such a manner that compression specimens can be made from the material remaining between the circular holes left in the bone by the shear plug cutter. These compression specimens, of diploë layer only, will be used to obtain true diploë specific weight values for use in the correlation of shear strength with specific weight. Because both the shear and compression specimens came from virtually the same region in the skull, it will also be possible to check the correlation between shear strength and compressive strength.



Figure 12 Photomicrograph of Failed Trabeculae of a Diplolæ Layer Compression Specimen (40X)

4. Composite Structural Testing of Skull Bone. (R. P. Hubbard)

The mechanical response of layered skull bone is being studied as an essential step in the development of a head injury model. Analytic mathematical models incorporating skull geometry and constituent material properties are being developed for determination of the mechanical response of skull bone. Development of mathematical models is based on available layered beam, plate, and shell theory and solutions. Because of relative simplicity, layered beams are more generally treated by models involving properties of the individual layers. Adequate solutions exist for layered plates using a less specific approach in which a layered plate is represented as a one layer plate with effective coefficients which account for the presence of a low stiffness core between stiffer facing layers. The effective stiffness coefficients must be determined either with layered beam theory or testing. Layered shell theory exists but no appropriate solutions have been found.

Because of relative simplicity, more complete analytical treatment, and relevance to plate and shell theory, skull bone beams are being tested in the bending fixture shown in Figure 13. Preliminary beam samples have been machined from embalmed calvaria and stored in an airtight plastic bag. Beam deflection is determined using a strain gaged cantilever beam. From the results of variable span three point bend tests using the same beam sample, the bending and shear stiffnesses of the skull beam can be determined. Preliminary beam test results indicate reasonable agreement with analytical values.

Beam test techniques can be used to study the bending stiffness and strength of skull sutures. Testing of layered skull plates and shells will follow beam testing.

From analytical layered structure models should come the link between constituent materials properties, geometry, and structural response of layered skull bone. Results from mechanical testing of skull samples will be compared with analytical results where possible and will yield understanding of phenomena which may not be adequately described by mathematical modeling.

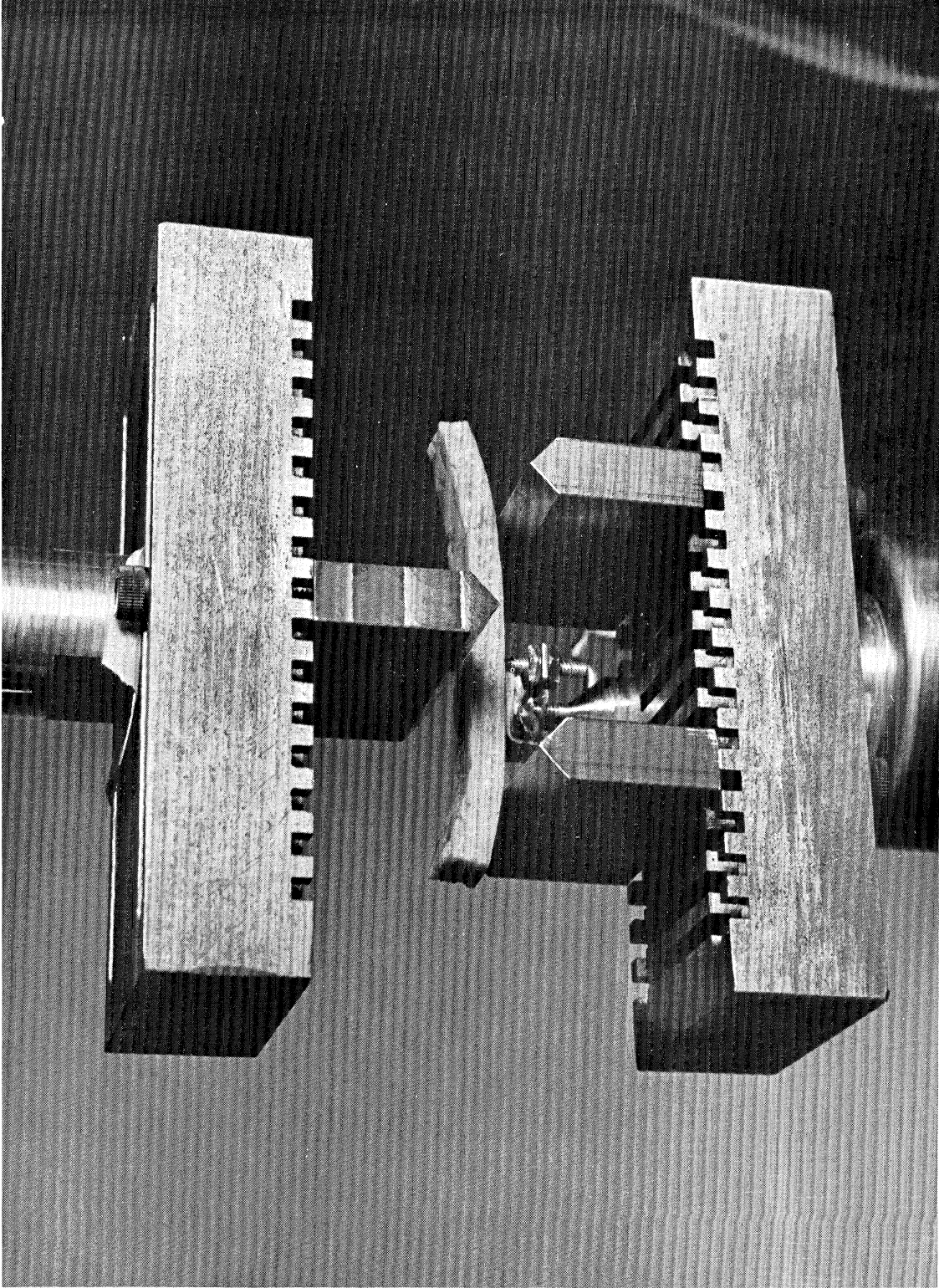


Figure 13 Adjustable Bending Apparatus and Deflectometer with A Beam of Embalmed Human Skull Bone.

B. Brain Tissue Tests. (Garnett T. Fallenstein and Verne D. Hulce, Dow Corning Corporation)

1. Introduction.

Dow Corning effort in the past six months consisted primarily of analysis of raw data obtained in previous tests of Rhesus monkey brain. The tests were performed utilizing the Dynamic Probe Apparatus (DPA), described in the eighteen-month report¹. Two additional tests were conducted in the period with the same basic assembly. Modifications to the system were limited to an improved operating table/test platform unit.

A method for reduction of non-linear data from the tests was devised which allows quantitative results to be extracted from the DPA results for the first time. A considerable amount of raw data was thus reduced and analyzed.

A preliminary test of the dynamic mechanical properties of in vitro human scalp was performed on the Dynamic Mechanical Apparatus (DMA).

Preliminary tests were also conducted on promising candidate substitute materials.

2. Equipment and Procedures.

a. DPA equipment.

A combination operating table/test platform unit was constructed for tests on live Rhesus monkeys. This unit replaces the previously used primate chair. The animal is placed in a prone position for testing, as contrasted with the sitting position dictated by the primate chair. This modification improves the test in that (1) less handling of the animal is required, (2) pre-test preparation time is reduced, and (3) the system provides for better manipulation of the DPA probe unit. Surgical procedures remained unchanged from those previously reported. All tests were conducted near the precentral gyrus as in previous tests. The basic DPA unit itself remained unchanged.

b. Data reduction.

The large majority of individual tests conducted on Rhesus monkey brain were at dynamic amplitudes of approximately $10\text{-}25 \times 10^{-3}$ cm. For this amplitude range, the force outputs obtained continued to be non-sinusoidal (non-linear) in nature, as has been previously observed. These data were reduced graphically. The portion of the sinusoidal input displacement between the least total brain deformation and the zero dynamic amplitude of the probe (i.e., the second quadrant of the sine input) was utilized. This portion of the corresponding force output appeared to approximate rather closely a sine wave and thus defined a linear component of the response to the displacement function. This total linear component of the force was resolved into sine and cosine components, yielding spring (k) and viscous loss (η) constants, respectively. The spring constant was converted into the dynamic elastic shear modulus (G') by utilizing the approximation

$$G' = \frac{k}{8r} \quad \text{where } r = \text{radius of the probe.}$$

For the DPA, this equation reduces to

$$G' = .727 k$$

This approximation has been utilized by von Gierke² in similar experiments and by Tangorra³, who derived the approximation in a different manner from von Gierke. Note that $\tan \delta$ is defined as the ratio of the maxima of viscous loss force to spring force ($\eta\dot{x}/kx$), whereas $\tan \delta$ for previous in vitro tests on the DMA was defined as G''/G' . It will be assumed that the two methods are equally valid.

3. Results.

a. DPA tests on silicone gels.

The DPA was used to test silicone gels at both 10 and 100 Hz. The 10 Hz. tests were conducted using the driving mechanism of the DMA in order to obtain a sinusoidal input. (The shaker of the DPA does not provide a sinusoidal signal in this low frequency range.) Standard DMA tests at near 10 Hz. were conducted on the same silicone sample (see Reference 1). The results indicated a rather close correlation in the dynamic elastic shear modulus, G' , but $\tan \delta$ was approximately 30% higher with the DPA probe/sample configuration when compared with the DMA tests.

<u>Test</u>	G' (dynes/cm ²)	G'' (dynes/cm ²)	<u>Tan δ</u>
DMA	3.8×10^4	1.1×10^4	.29
DPA	4.2	1.6	.39

Another silicone gel, originally utilized to test the DPA during early development, was tested some six months later under the same conditions. The test frequency was 100 Hz. The results were within 10% of each other, a very good correlation, as the tests were entirely separate and were conducted on adjacent, but not identical, test sites from the same sample (see Figure 14).

b. DPA tests on dog brain (in vitro).

Tests similar to the low frequency (10 Hz.) tests of gels were conducted on an in vitro dog brain hemisphere. The surface of the hemisphere was kept moist with isotonic saline solution. The dynamic amplitudes and static deformations were within the ranges utilized on in vivo tests of Rhesus brain at 80-100 Hz.

The results indicated linear responses whereas analogous tests on Rhesus brain at higher frequency yield markedly non-linear responses. Also, the increase of G' with increasing static deformation is not so pronounced. A best fit of G' versus static deformation was obtained using a linear plot (see Figure 15).

c. DPA tests on Rhesus monkey brain.

Raw data from some 42 individual DPA tests on six Rhesus monkey brains were reduced by the graphic process described in Section 2b. Both in vivo and post-mortem tests were analyzed. Blood pressure was varied in a controlled manner in a small number of tests. The resulting G' for each test was plotted against static deformation, a common variable. Figure 16 shows the total results. Figure 17 shows the results from two individual test series (i.e., all tests from each of two separate Rhesus brains). These tests, deemed to be the most reliable, yield good fits when G' is plotted versus static deformation on a semi-log graph.

A correlation coefficient matrix was run in order to obtain the significance of supposed variables (see Table III). Forty-two sets of high-amplitude data were used. Note that correlation was obtained for k versus static deformation with a probability of 99%. The viscous component, η , versus static deformation yielded a similar coefficient. On a trial basis, judging from Figure 17 and evidence of Franke⁴, it was assumed that the indicated relation between k or G' and static deformation was exponential:

$$G' = Ae^{Bx} \quad \text{where } x = \text{static deformation.}$$

Least square regression curves were calculated fitting G' values for the linear portions of the force curves to this relation. A first approximation was obtained using all of the above data. Then all data that could reasonably be assumed erroneous due to either (1) lack of control of variables or (2) lack of definition of variables were excluded. Finally, regression fits were obtained for the two test series of Figure 17 where good relationships were evident visually. The regression curves are shown in Figures 18 and 19 along with their correlation coefficients r , and the number of data sets utilized for the computation.

The regression equations have y-intercepts between 2.1 and 5.1×10^4 dynes/cm². This yields G' at zero deformation in the range of $(3.6 \pm 1.5) \times 10^4$ dynes/cm².

d. DMA tests on human scalp.

A sample of human scalp was tested in vitro utilizing the DMA. The sample geometry was that routinely used for testing elastomeric samples. (A rectangular bar specimen is mechanically grounded at both ends, with its major axis normal to - and its major plane parallel to, the DMA driver shaft. The center is clamped to the DMA driver shaft. This, in effect, creates two shear specimens.) The test frequencies were near 10 Hz., similar to those employed in testing brain tissue. Testing procedures were similar also. In this preliminary test G' measured 14×10^4 dynes/cm², and G'' 4×10^4 dynes/cm², yielding a $\tan \delta$ of .29.

4. Summary and Conclusions.

Though a large degree of variability is evident in the overall DPA test data, and in some cases within tests on a single brain, there does appear to be a relationship between the apparent G' and the probe static deformation. In cases where both in vivo and post-mortem tests were conducted, the variability between the two types of tests was less than the general data scatter.

The overall variability in later tests was less than that encountered in earlier, more exploratory tests. A possible cause of some of the data scatter is long-term motion of the brain within the skull after positioning of the probe. If such a motion is present, however, it is apparently random, as tests conducted immediately after a static deformation determination do not correlate better than the data taken as a whole.

The fact that G' increases with static deformation is not contrary to previous work in the field of biomechanics. Franke⁴ and von Gierke² both noted similar increases in studies of the impedance of the human body surface. von Gierke noted that one must be aware of variations in the modulus due to static deformation and Franke plotted stiffness versus static deformation, obtaining a relation similar to that obtained in the 80-100 Hz. tests of Rhesus brain.

The G' obtained in the DPA tests results from the apparent spring constant (k) over a small dynamic amplitude superimposed on a relatively large static deformation. The spring constant thus obtained is a tangent value. That the tangent spring constant varies with static deformation defines a non-linear force-deformation relationship for the DPA probe on brain tissue. Also, using the observed magnitudes of change in the spring and viscous loss constants with static deformation, it can be shown that non-linear force outputs of the type observed experimentally will result from sinusoidal displacement inputs.

Note that in similar tests of brain material at 10 Hz., the force response was linear. However, the G' versus static deformation plot was linear, compared to the exponential plot for 80 Hz. tests.

Tests conducted on silicone gels have not yielded an exponential relationship for k versus static deformation. Rather, k increases linearly but with a smaller slope than any encountered with tests of brain tissue. Non-linearity has been obtained in a subjective test of a gel-filled balloon, diameter about 3 cm., slightly pressurized. Possible causes include pre-stressing the membrane covering (which had a small radius of curvature) and pressurizing the gel. Similar balloons filled with either water or air exhibited linear responses.

The data thus far obtained tends to indicate that the dynamic shear spring modulus G' lies in the lower 10^4 dynes/cm² range for tests conducted in the 80-100 Hz. frequency range. There is a large variability in the data and any changes from in vivo to post-mortem are less than the test variability encountered.

It is felt that more testing of a similar nature is necessary before a modulus value can be quoted with reasonable certainty and with a reasonable tolerance. Such testing should also lead to a more precise determination of change in properties at death.

References

1. Highway Safety Research Institute (The University of Michigan), (1969), "Eighteen Month Report on Contract PH 43-67-1136," Appendix B.
2. von Gierke, H. E., Oestricher, H. L., Franke, E. K., Parrach, H. O., and von Wittern, W. W., (1952), "Physics of Vibrations in Living Tissues," J. Appl. Physiol., 4, 886-900.
3. Tangorra, G., (1963), "The Indenter Hysteresimeter for Testing Dynamic Properties," Rubber Chem. and Tech., 4, 1107-1118.
4. Franke, E. K., (1951), "Mechanical Impedance of the Surface of the Human Body," J. Appl. Physiol., 3, 582-590.

TABLE III. RESULTS OF CORRELATION MATRIX FOR VARIABLES IN DPA TESTS OF RHESUS MONKEY BRAIN

	State	Blood Pressure	Static Deformation	Frequency	η	k	Tan δ	Dynamic Amplitude
State	1							
Blood Pressure	-.824	1						
Static Deformation	-.060	-.154	1					
Frequency	-.185	.043	-.131	1				
η	.180	-.272	.532	.183	1			
k	.146	.219	.420	.360	.918	1		
Tan δ	-.236	.114	-.136	.641	-.038	-.119	1	
Dynamic Amplitude	-.137	.272	.060	-.075	-.501	-.660	-.253	1

$d_f = 40$ $P_{.05} = .304$ $P_{.01} = .393$

Figure 14 G' versus Static Deformation.
100 Hz. DPA Test of a Silicone Gel.

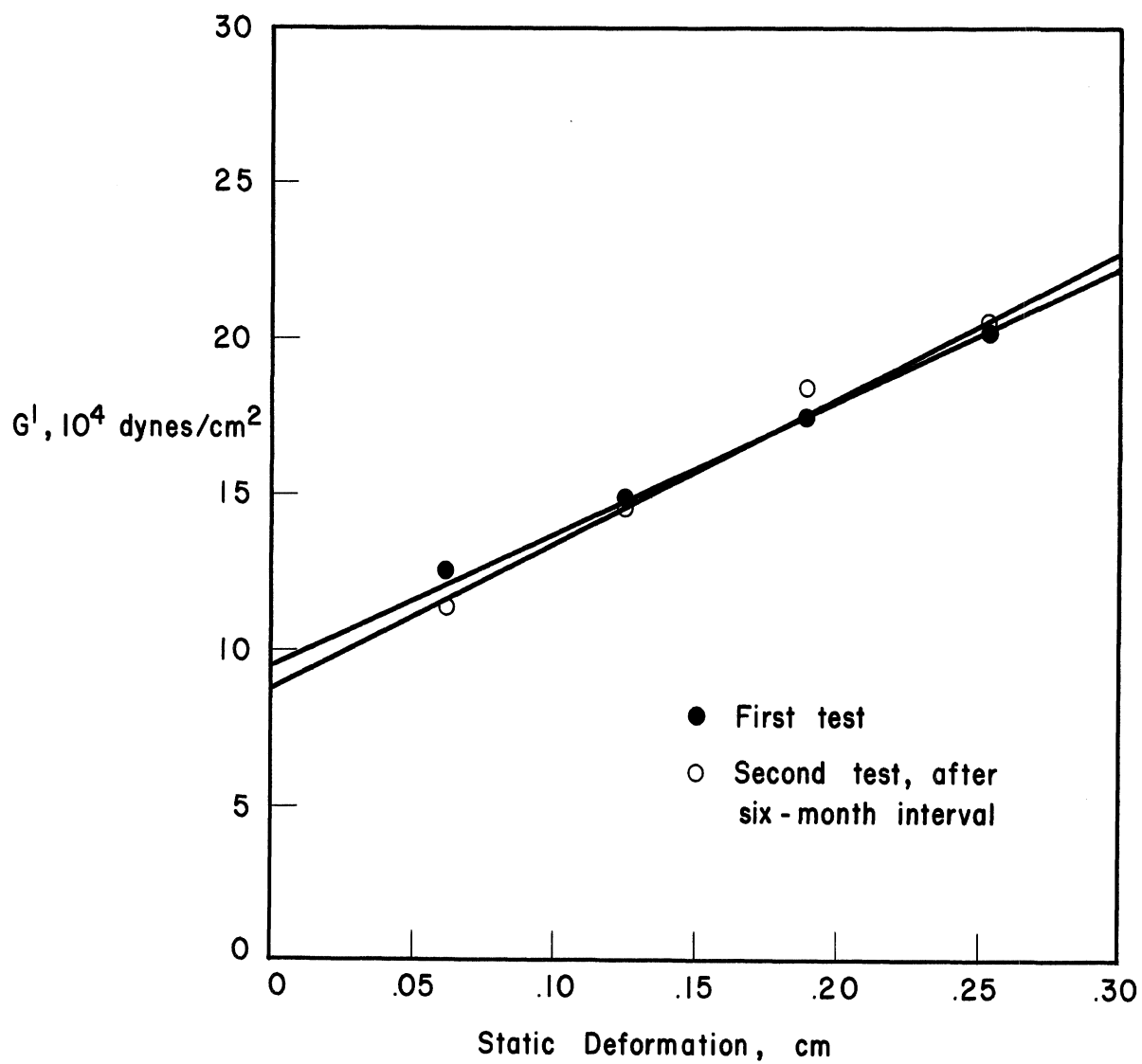


Figure 15 G' versus Static Deformation of Dog Brain.
10 Hz. DPA Test.

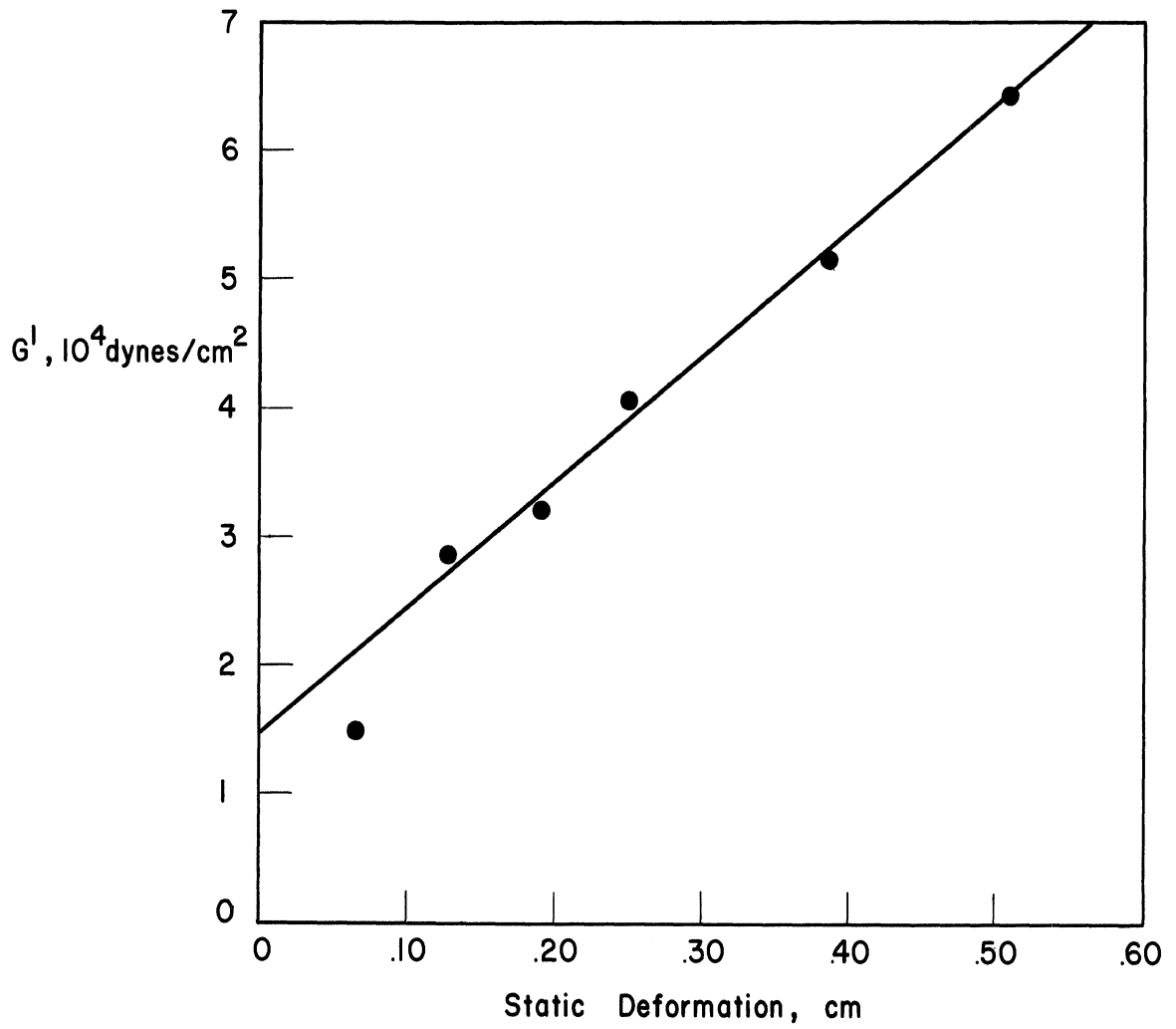


Figure 16 G' versus Static Deformation of Rhesus Monkey Brain.
All High-Amplitude Tests Reduced by Graphic Method.

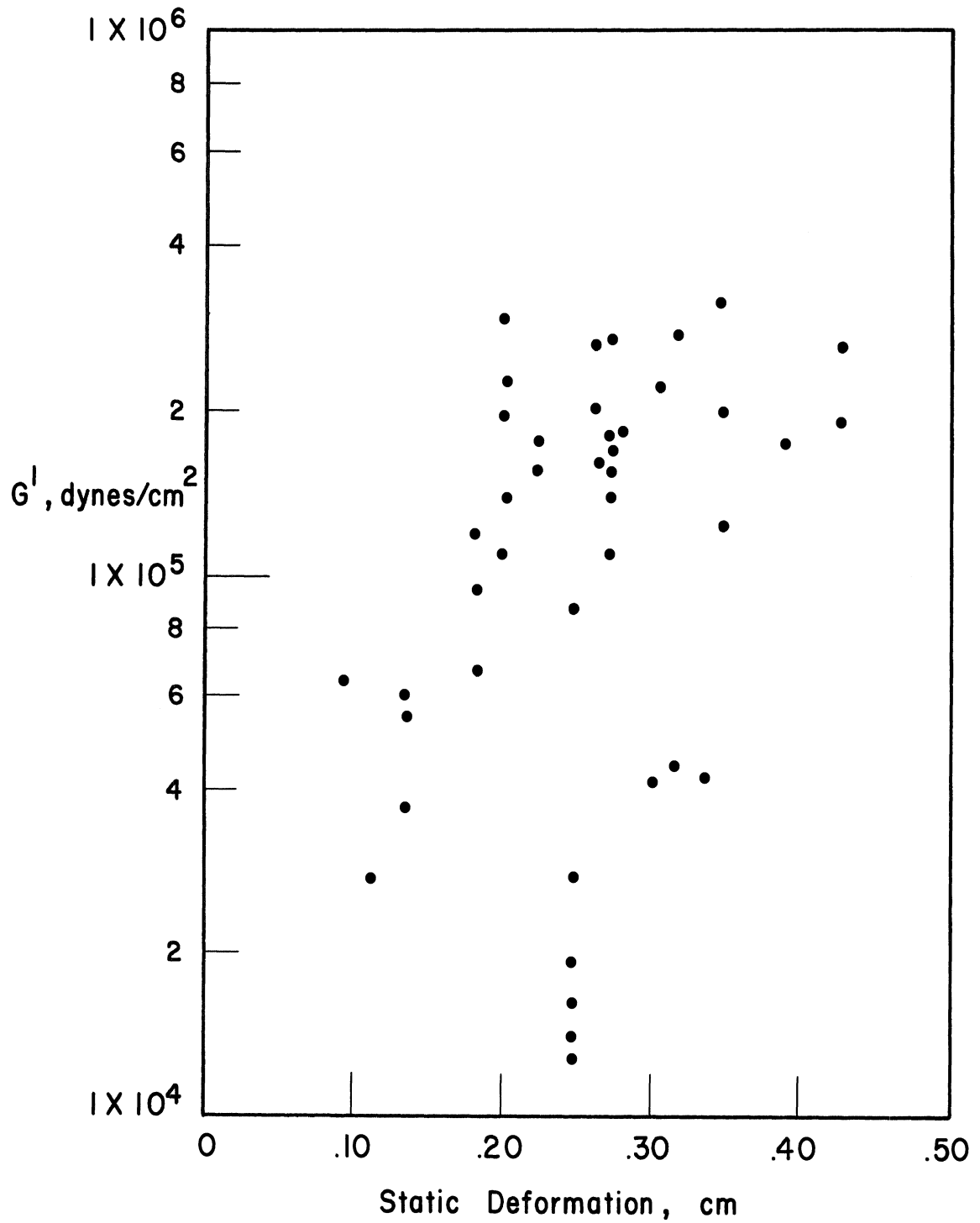


Figure 17 G' versus Static Deformation of Rhesus Monkey Brain.
Two Best Individual Brains.

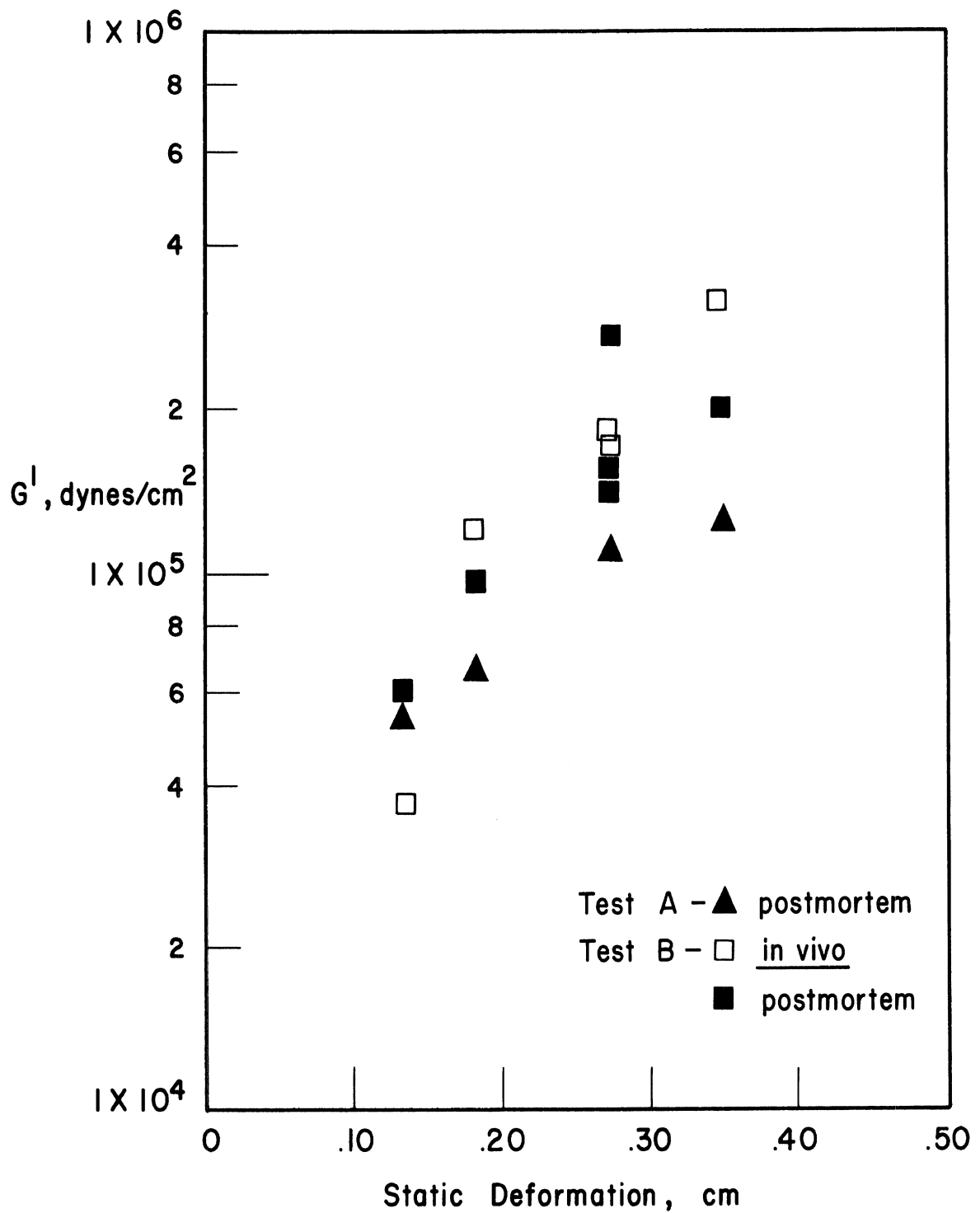


Figure 18 Least Squares Fits of DPA Data. G' versus Static Deformation of Rhesus Monkey Brain. First and Second Approximations.

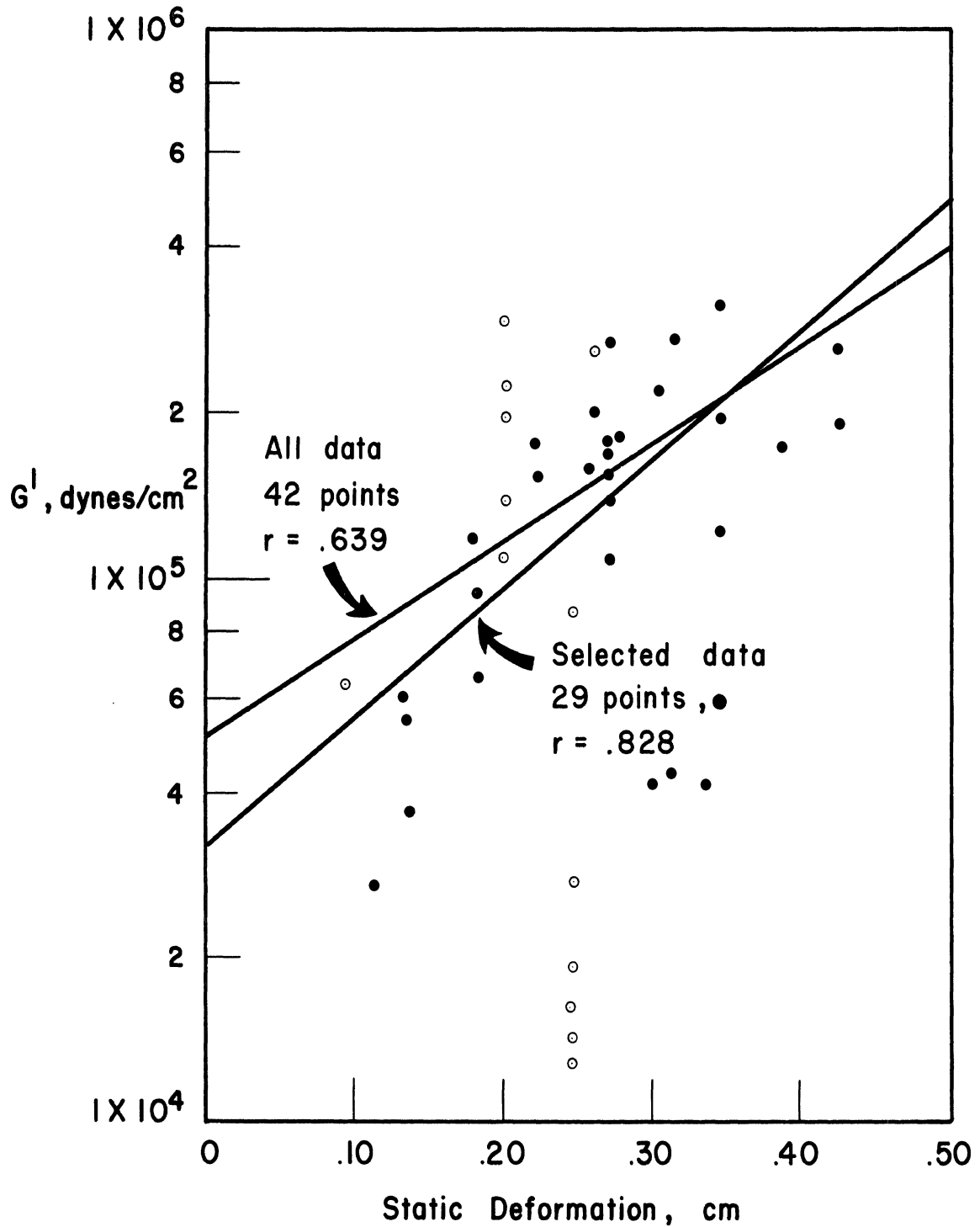
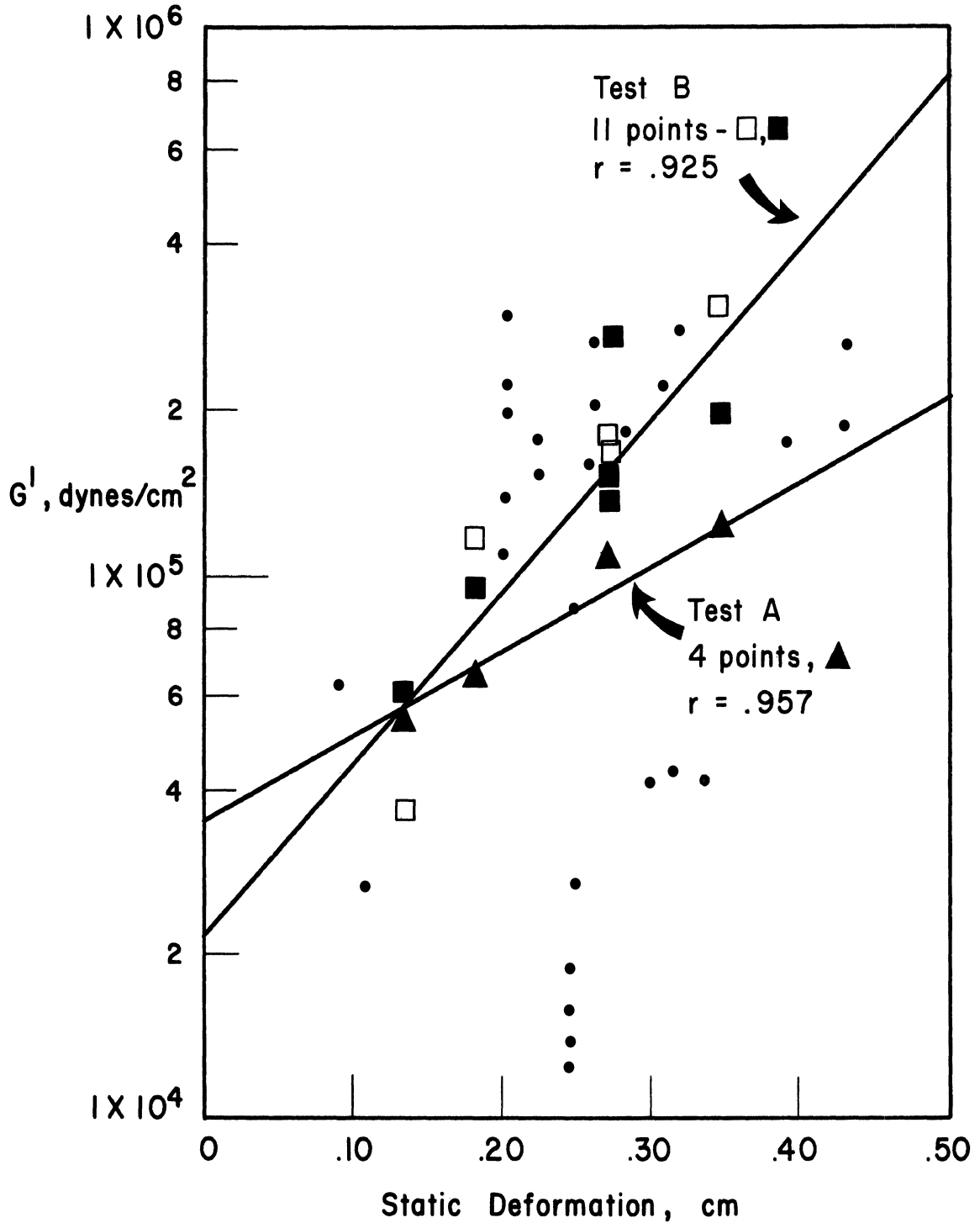


Figure 19 Least Squares Fits of DPA Data. G' versus Static Deformation of Rhesus Monkey Brain. Fits for Each of Two Best Tests.



C. Other Soft Tissue Tests

1. Dura Mater Tests (J. W. Melvin and I. Barodawala)

In the past six months 100 tension tests of fresh human dura mater have been performed. Eighty of the tests were performed at a nominal strain rate of 0.061 sec^{-1} and twenty were performed at a nominal strain rate of 0.61 sec^{-1} . The tests were performed in the Instron universal testing machine. The test specimen shape is a specially made dumbbell specimen which is 2.25 inches long with a reduced gage length section 0.25 inch wide and 0.75 inch long. This specimen size allows up to eleven specimens to be cut out of a typical sample of dura mater. The dura mater is obtained at autopsy and placed in a jar of saline solution. If the specimen cannot be tested immediately, it is stored in the saline solution in the refrigerator. An Instron load cell of 1000 lbs. capacity is used to indicate the load on the specimen and the strain in the specimen is measured by the phototransistorized optical extensometer shown in Figure 20 and described in the eighteen month report. The load cell is displayed versus the strain on an oscilloscope and the resulting curve is photographed for later analysis.

The macrostructure of dura mater, in the regions relatively free from large blood vessels, appears to be a membrane with notable directions of fiber reinforcement. Further examination indicates that the direction of apparent fiber orientation when viewed on the outside surface of the material is different from that when viewed on the inside. Rough measurement of the angle between these two

directions shows it to be about 70° . Some X-ray diffraction analyses run on samples of dura mater also indicate two directions of orientation about 70° apart. The inner layer of dura mater may be peeled off and it is much thinner than the remaining dura mater. Because of the highly structured nature of dura mater two procedures have been incorporated into the test program. One is close histological examination of the material both before and after testing. The samples representing before test conditions are taken near the site of the specimen and parallel to the test section. The test section of the specimen itself is used as the after test sample. The samples are stained, embedded in paraffin, sectioned into 10 micron thicknesses and mounted. Figure 21 shows a typical before test sample. Note the short range alignment of fibers and the longer range random orientation. A tested sample is shown in Figure 22. The orientation in the test section is quite pronounced. The second procedure for study of orientation effects is to take specimens in three different directions in the dura mater. These directions are the longitudinal direction, (parallel to the sagittal plane), the transverse direction (perpendicular to the sagittal plane), and the diagonal direction (roughly 45° to either of the other two directions). These directions are noted in the test data.

Analysis of the data obtained to date is shown in Table IV, and in Figures 23 and 24. The central curve in each band is the mean and the bounds of the bands are the standard deviations. The strain at failure is quite similar in both of the test directions shown but in

Figure 16, there are noticeable modulus and strength differences. Dura mater seems to exhibit an initial limit strain such as skin does, but it is only about one-tenth the magnitude of the values associated with human skin. The data shown in Figure 24 can only be considered tentative because of the small sample number.

2. Scalp Tests

A limited number of fresh human scalp tests have been performed in the last six months. With the exception of some cyclic shear tests on scalp, which are reported under the Dow-Corning brain testing section of this report, all the tests on scalp were radial compression tests on composite samples. The scalp samples were taken at autopsy in the form of a strip about 3 inches long and 0.25 to 0.50 inch wide. The sample was placed in saline solution and then tested immediately or stored in a refrigerator until it could be tested. The specimens were roughly rectangular and their dimensions depended directly on the width of the sample and the thickness of the scalp. The fatty subcutaneous layer was left intact on the specimens. The nominal strain rate in the tests was about 0.2 sec^{-1} .

An aggregate compressive stress strain curve for nine tests is shown in Figure 25. The appreciable strain accumulation with zero or near zero load corresponds to compressing of the fatty subcutaneous layer. Also shown in Figure 25 is an experimental synthetic material developed by the automotive industry to simulate scalp for comparison.

TABLE IV SUMMARY OF DURA MATER TENSION TESTING

Strain Rate sec	Specimen Orientation Relative To Sagittal Plane	Mean σ psi	Mean E psi	Standard Deviation σ psi	Standard Deviation E psi	Total No. of Specimens	Total No. of Persons
0.061	Longitudinal	736.8	5,046	282.6	2242	12	5
0.061	Transverse	928.1	6,094	308.6	2187	7	4
0.061	Diagonal	1,219	7,565	459.7	4089	24	8
0.61	Longitudinal	1,318	12,008	429.1	5492	7	3
0.61	Diagonal	1,092	8,856	453.9	3902	5	2

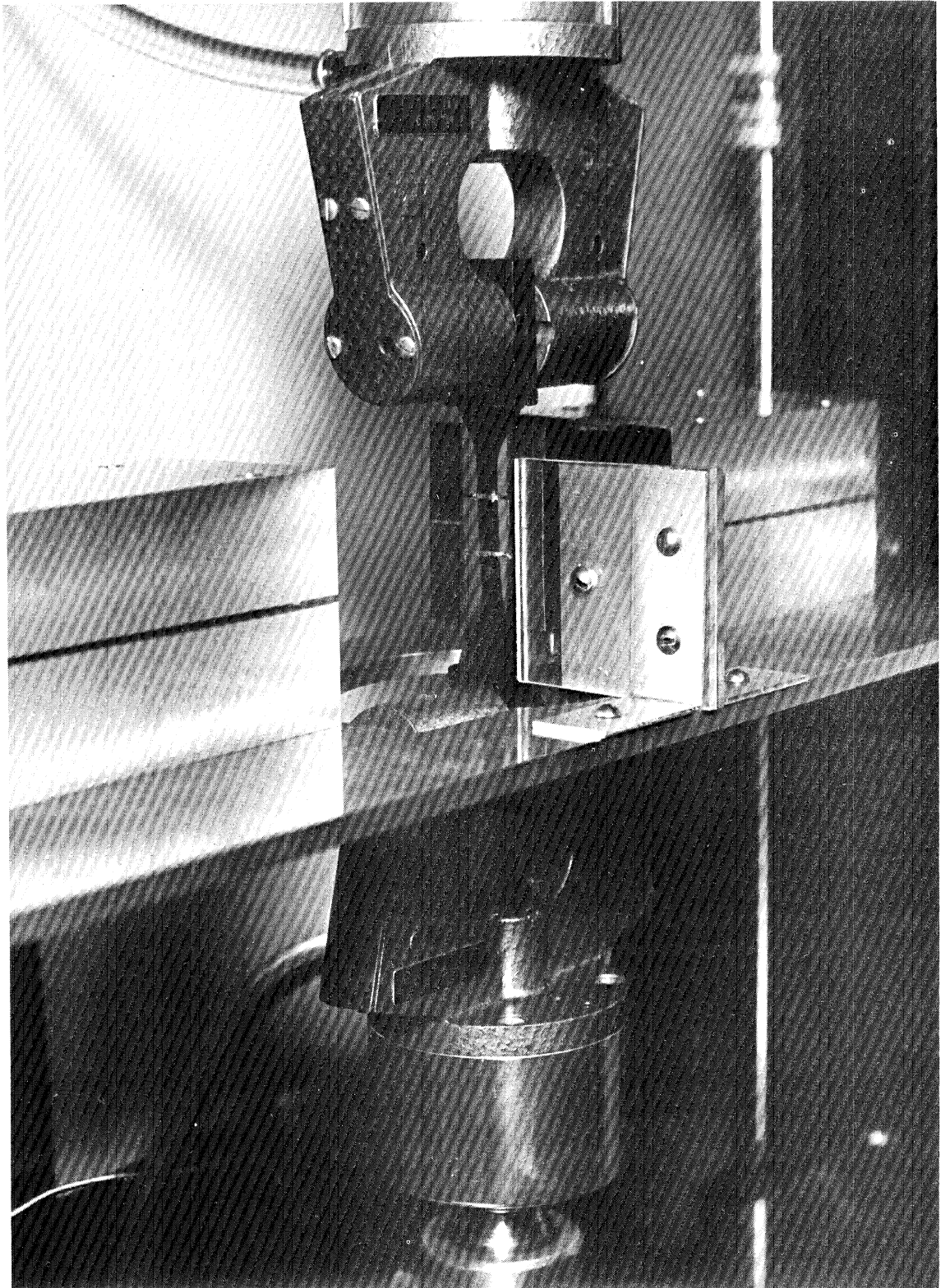


Figure 20 Phototransistorized Optical Extensometer with a Rubber Test Specimen in Place

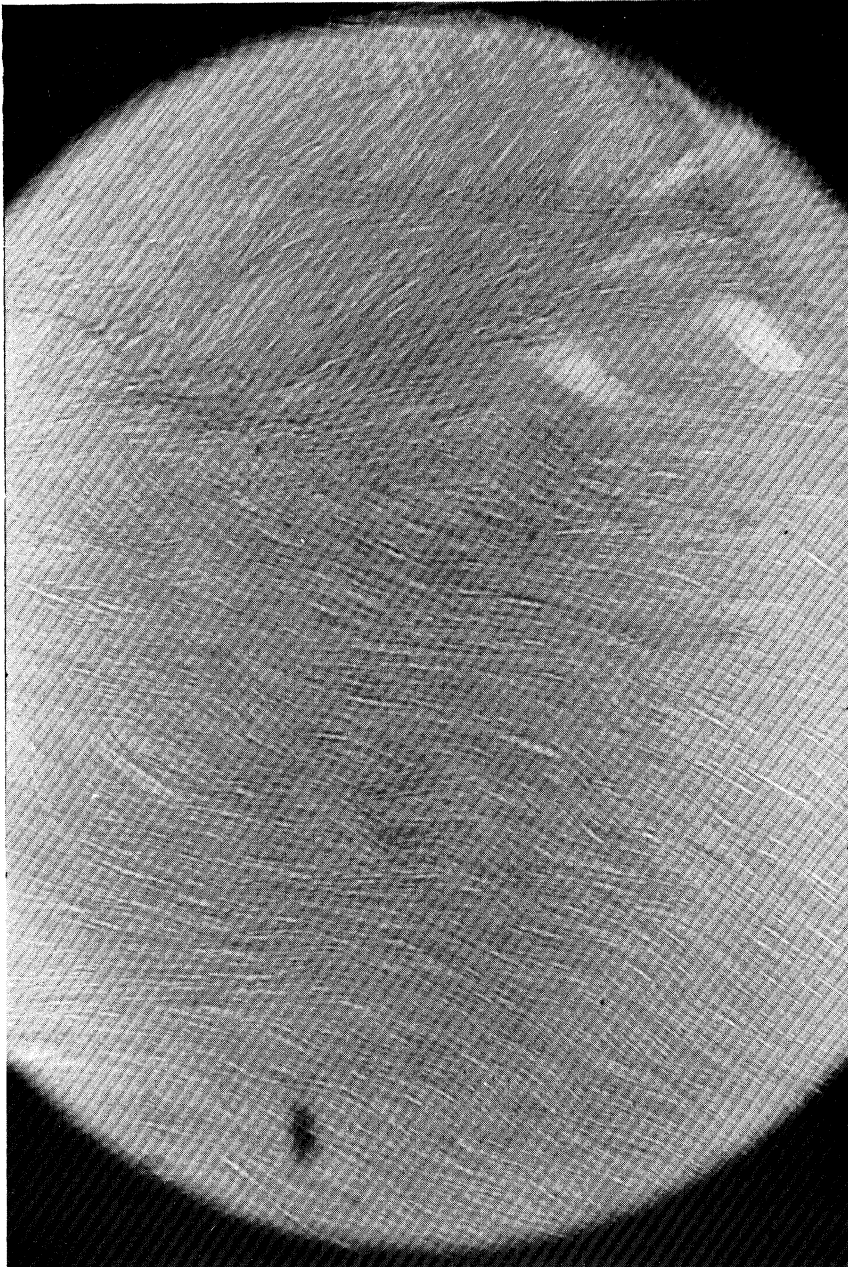


Figure 21 Untested Dura Mater (100X)

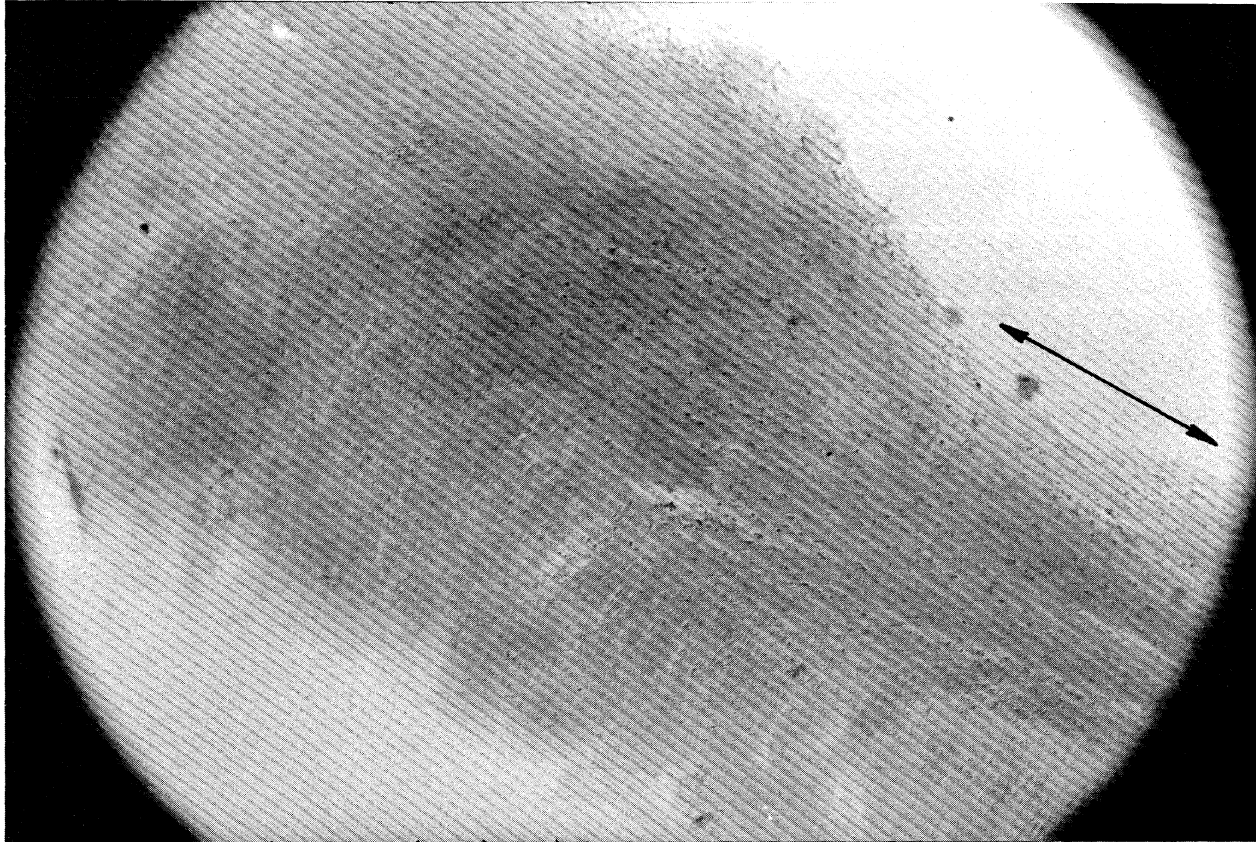
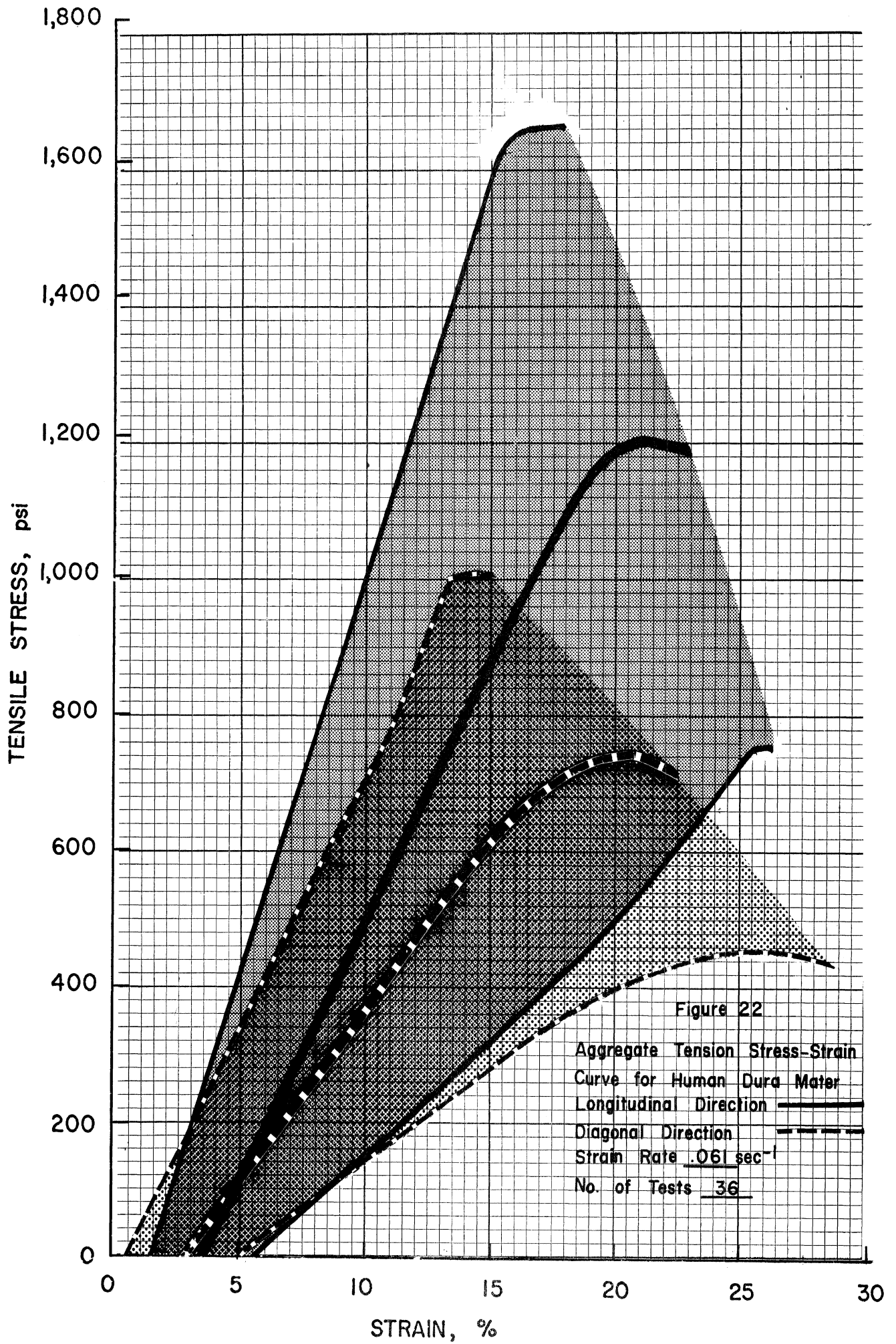


Figure 22 Tested Dura Mater (Arrow Indicates Test Direction) (40X)



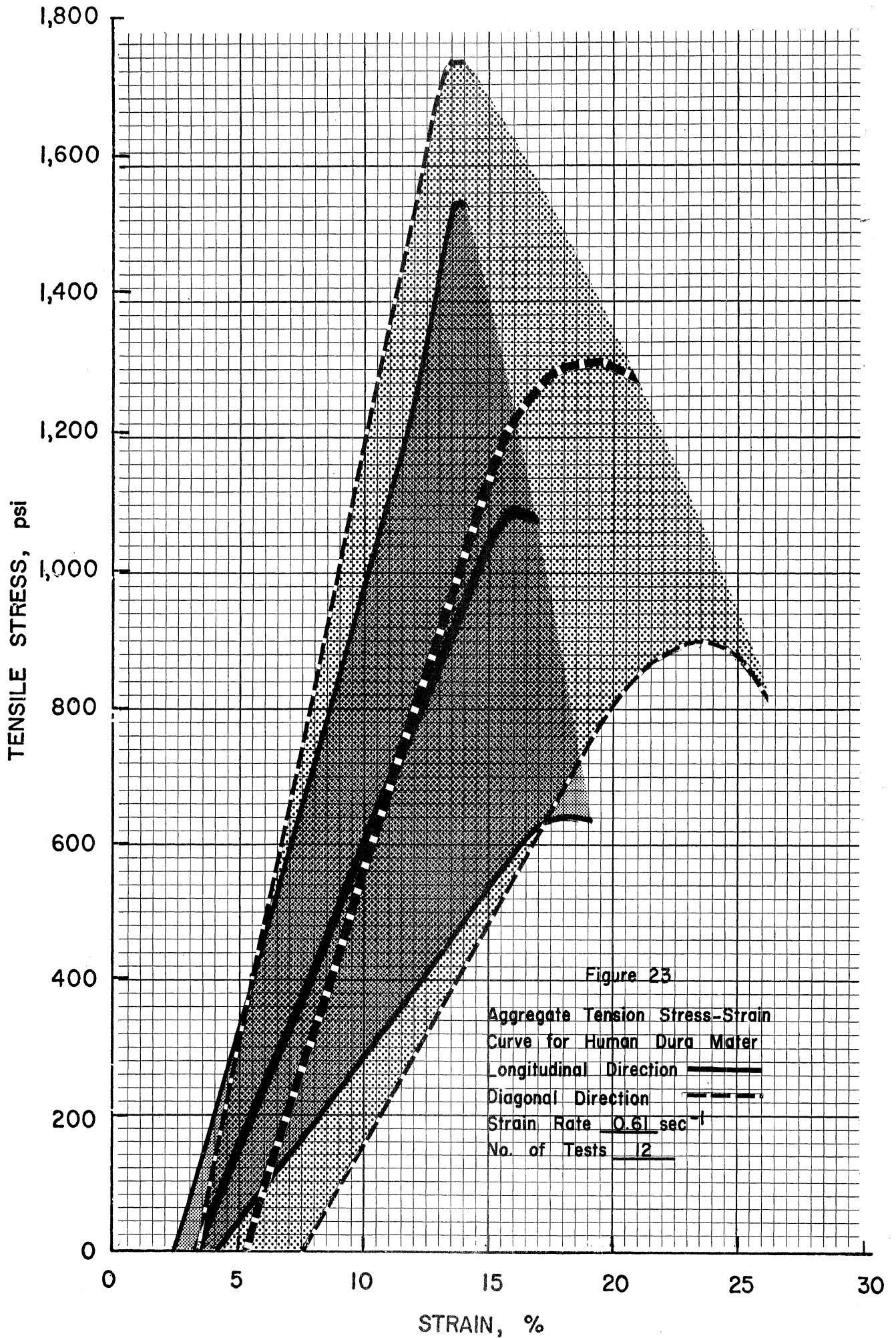
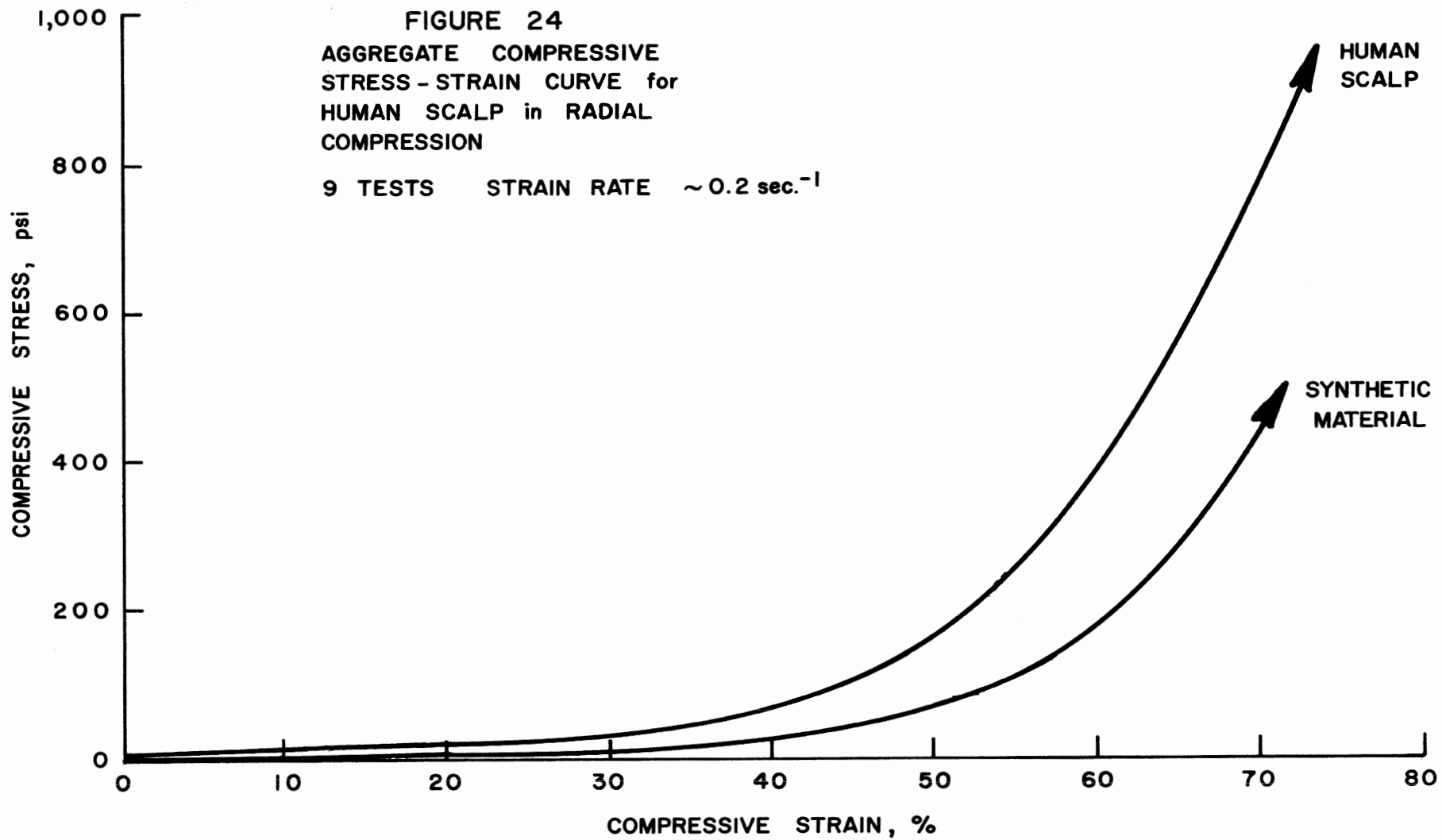


FIGURE 24
AGGREGATE COMPRESSIVE
STRESS-STRAIN CURVE for
HUMAN SCALP in RADIAL
COMPRESSION

9 TESTS STRAIN RATE $\sim 0.2 \text{ sec.}^{-1}$



III. ANALYTICAL PROGRAM Ali E. Engin

In the eighteen-month report the basic course of theoretical research was outlined. As previously stated, the analytical program was divided into two very closely related parts. These parts are:

- 1) Development of meaningful constitutive equations describing the physical properties of the various tissues of head.
- 2) Analysis of progressively more sophisticated theoretical head injury models.

In order to construct theoretical head injury models realistically, the knowledge of part 1 should precede that of part 2. Since the last report most of the analytical effort has been directed to part 1. Among the various approaches considered for the development of the constitutive equations are (a) empirical methods, (b) theoretical methods, and (c) combination of empirical and theoretical methods. To see the previous work done in this area using these methods, an extensive survey of the literature has been made. A summary of some of the representative papers on the experimental work done for various soft tissue was prepared and it will be presented in a later report.

The leading empirical method is to find an approximating formula for the experimental data. For this there are two approaches possible. One is to have the approximating function pass through the experimentally observed points. The other approach is to have the approximating function retain some properties of the data, such as the shape of the curve, and to have it pass as close as possible but not necessarily

through the original data. This is usually acceptable when dealing with experimental data which are subject to a certain amount of error. Method of Least Squares of Linear Regression equations are approximating formulas belonging to the latter approach. At the present time, a computer program using regression analysis is available to supply an empirical uniaxial constitutive equation for a given experimental data. This equation represents a curve in two-dimensional space. When the data for biaxial tests become available, the ideas used for the uniaxial constitutive equations can be projected to obtain biaxial constitutive equations with the help of a technique which already exists at the Computing Center of The University of Michigan. A biaxial constitutive equation geometrically represents a surface in three-dimensional space. A very essential advantage of the empirical equations is that previously specified material behavior such as elastic, visco-elastic, elastic-plastic, etc., is not required.

Most of the theoretical papers on the constitutive equations are on the philosophy of these equations and they have been written with the language of general tensors or functionals. From the application point of view they can be considered useless because of the gap between the theoreticians and the experimentalist, and experimental difficulties especially dealing with biological materials. Rivlin and his associates in the field of rubber elasticity and Y. C. Fung in biomechanics made some contributions to close the gap. The concept we are following is to develop a theory which results in experimentally possible analysis to determine the constitutive equations. Essentially, a modification

for Green's approach to constitutive equations is being considered. According to this approach a constitutive equation can be derived from an internal energy function which is assumed to be a function of the strain only. Modification being considered is the inclusion of strain-rate as well as strain for the argument of internal energy function. When one considers that most of the biological materials exhibit nonhomogenous, anisotropic and nonlinear viscoelastic characteristics, the great complexity of the problem of mechanical property determination is obvious.

An example of the combination of empirical and theoretical methods is given in the Appendix A "A Mathematical Model to Determine Viscoelastic Behavior of In Vivo Primate Brain." This paper illustrates how one can obtain complex dynamic shear modulus of in vivo brain from the combined relationships of theoretical analysis and experimental data. From the theoretical mechanics point of view, the problem being considered is that of the steady state response characteristics of a solid sphere of linear viscoelastic material whose mating surface with the rigid container is free from shear stresses. The external load is taken to be a local radial harmonic excitation. This is a theoretical model for an experimental setup consisting of an electromechanical device with a small driving point impedance probe which is placed in direct contact with the pia-arachnoid through a hole in the skull of a Rhesus monkey. In the theoretical analysis, the response of the elastic material is determined first; later elastic response solution is converted to viscoelastic response solution through the use of the elastic-viscoelastic correspondence principle

applicable to steady state oscillations. The paper is concluded with a discussion of a method to determine the complex dynamic shear modulus, G^* , of in vivo primate brain.

When the knowledge of G^* as a function of frequency is obtained it can be used for a mechanical property of brain in the more complex head injury models. At the present time various head injury models are being evaluated for feasibility. One of them is concerned with the impulsive response of a viscoelastic material filled in a rigid spherical shell. This model can be viewed as a further extension of the work done by Anzelius and Güttinger who treated the impulsive response of inviscid, irrotational fluid filled in a rigid spherical shell. The other model under consideration takes into account the effect of the cranial-cervical junction on the stress distribution within the skull and the pressure gradients in the brain when the head is subjected to impact or impulsive loads. It is felt that analysis of each new model with improved constitutive equations will be useful for the formulation of a much more complex head injury model such as an irregularly shaped shell structure filled with viscoelastic material.

APPENDIX A

A MATHEMATICAL MODEL TO DETERMINE VISCOELASTIC
BEHAVIOR OF IN VIVO PRIMATE BRAIN

by

Ali E. Engin
Han-chou Wang

Highway Safety Research Institute
The University of Michigan
Ann Arbor, Michigan 48105, U.S.A.

ABSTRACT

Determination of mechanical properties of the constituents of the head is very essential for the construction of various theoretical and experimental head injury models. This paper represents a mathematical model for the evaluation of viscoelastic behavior of in vivo primate brain. From theoretical mechanics point of view, the problem being considered is that of the steady state response characteristics of a solid sphere of linear viscoelastic material whose mating surface with the rigid container is free from shear stresses. The external load is taken to be a local radial harmonic excitation. First, the response of the elastic material is determined; later elastic response solution is converted to viscoelastic response solution through the use of the correspondence principle applicable to steady state oscillations. The paper is concluded with a discussion of a method which enables one to determine the complex dynamic shear modulus of in vivo primate brain.

INTRODUCTION

Vulnerability of human head and the resulting fatalities from various injuries to the head is a well-established fact. The gravity of the situation attracted many investigators from both experimental and theoretical fields of physical sciences. Previous research to give a proper description of the head injury has been either on determination of mechanical properties of the constituents of the head or on analyses of various theoretical head injury models. The investigations on these two categories are numerous. Only a few representative ones will be mentioned here.

Among the numerous theories proposed for the brain damage, the theory mainly advocated by Holbourn (1943) and theory supported by the mathematical analyses of Anzelius (1943) and Güttinger (1950) received the most attention. According to Holbourn the main cause of brain damage is the shearing effect produced by the severe deformation or fracture of the skull at the vicinity of the impact to the head or rotations of the brain within the skull. Anzelius and Guttinger considered the effect of a sudden impulsive load on a mass of inviscid fluid contained in a rigid closed spherical shell (or container). Their formulations are essentially identical and involve an axisymmetric solution of the wave equation in spherical coordinates. They concluded that an initial compression wave arises from the point of impact (coup), and due to the rigidity of the shell, instantaneously a tension (rarefaction) wave is emitted from the counterpole, both travelling towards the geometric center of the system. The collision (superposition) of the two waves at the center produces large pressure gradients, which was considered to be the cause of brain damage. Hayashi (1968) treated a one-dimensional version of the Anzelius-Guttinger model. His model consists of a rigid vessel (skull) containing inviscid fluid (brain). The vessel is attached to a linear spring, which

represents the composite elastic properties of the skull, scalp, etc. Approximate solutions were obtained for the limiting cases of very soft and very hard impacts. Although this simple model has the advantage of being easy to interpret, it has the similar shortcomings of the Anzelius-Guttinger model. Some of these shortcomings are: (a) due to rigidity and geometrical assumption, there is no way one can determine the possible locations of skull fracture and (b) the effects of skull deformation on the intracranial pressure distribution can not be determined. Recently, Engin (1969) by obtaining analytical and numerical solutions for the dynamic response of a fluid-filled elastic spherical shell removed the major restrictions of previous models. His model consists of elastic spherical shell filled with inviscid compressible fluid. The shell material and fluid are considered to be homogenous and isotropic. The loading pattern is taken local, radial, impulsive and axisymmetric. Since the load is applied locally the combined linear shell theory which includes membrane and bending effects of the shell has been used for the proper description of the wave propagation. The conclusions of his paper include the possible locations of brain damage and skull injury on the basis of the numerical computations.

Further extensions of Engin's model is possible if one knows the viscoelastic properties of brain; with this knowledge one can replace the inviscid fluid occupying the interior space of the shell with a viscoelastic material. In literature, there are only four papers on the mechanical properties of brain. Franke (1954) determined the coefficient of shear viscosity from impedance measurements of a glass sphere vibrating within fresh pig brain. Creep experiments were performed by Dodgson (1962) and Koeneman (1966) who also studied dynamic cyclic properties from rabbits, rats, and pigs. Recently, Fallenstein, et. al (1969) developed an electromechanical device with a small

driving point impedance probe which was placed in direct contact with the pia-arachnoid through a hole (diameter is approximately 1/8 inches) in the skull. By means of this apparatus in vivo as well as in vitro tests on Rhesus monkeys were performed. In this paper, we will give the theoretical analyses of such a test conducted on the brain. The theoretical model for the mathematical analyses is shown in Fig. 1. From mechanics point of view, the problem being considered is that of the steady state response characteristics of a solid sphere of linear viscoelastic material whose mating surface with the rigid container is free from the tangential shear stresses. In particular, we will be interested in the response of the viscoelastic material to a local radial harmonic excitation. First, the response of the elastic material will be determined; later elastic response solutions will be converted to viscoelastic response solutions through the use of the elastic-viscoelastic correspondence principle applicable to steady state oscillations. We will conclude this paper with a discussion of a method which enables one to determine the linear viscoelastic parameters of the brain.

THEORETICAL ANALYSES

As mentioned in the Introduction, the theoretical analyses of the model in consideration will be given in two parts, namely; a) Elastic Response, and b) Viscoelastic Response. We shall use the same model, Fig. 1, for both parts; the only difference will be in the type of material which occupies the rigid spherical shell.

a) Elastic Response The linear equations of motion of an elastic medium, in vector form, are given by Fung (1965)

$$(\lambda + 2G)\nabla(\nabla \cdot \bar{u}) - 2G\nabla \times \bar{\omega} = \rho \frac{\partial^2 \bar{u}}{\partial t^2} \quad (1)$$

where \bar{u} and $\bar{\omega}$ represent the displacement and rotation vectors respectively, ρ is the mass density of medium, λ and G are the elastic material constants.

These equations can be expressed in spherical coordinates, Fig. 2, and introduction of axisymmetry and precluding torsional displacements mean

$$\frac{\partial v}{\partial \theta} = 0 \quad , \quad v = 0 \quad , \quad (2)$$

where v is the displacement component in the θ direction. The remaining components of the displacement vector are along ϕ and along the radial coordinate, r , and they are u and w respectively. In view of conditions (2) the Eq. (1) yields the following two equations in spherical coordinates

$$(\lambda + 2G) \frac{\partial \Delta}{\partial r} - \frac{2G}{r \sin \phi} \frac{\partial}{\partial \phi} (\omega_{\theta} \sin \phi) = \rho \frac{\partial^2 w}{\partial t^2} \quad , \quad (3)$$

$$\frac{(\lambda + 2G)}{r} \frac{\partial \Delta}{\partial \phi} + \frac{2G}{r} \frac{\partial}{\partial r} (r \omega_{\theta}) = \rho \frac{\partial^2 u}{\partial t^2} \quad (4)$$

where Δ is the cubical dilatation defined by

$$\Delta = \nabla \cdot \bar{u} = \frac{\partial w}{\partial r} + \frac{2w}{r} + \frac{1}{r} \frac{\partial u}{\partial \phi} + \frac{\cot \phi}{r} u \quad , \quad (5)$$

and ω_θ is a component of $\frac{1}{2}(\nabla \times \bar{u})$ and its value is

$$\omega_\theta = \frac{1}{2r} \left[\frac{\partial(ru)}{\partial r} - \frac{\partial w}{\partial \phi} \right]. \quad (6)$$

The equations of motion (3) and (4) can be uncoupled by assuming the displacement vector in the form of the gradient of a scalar function, ϕ , plus the curl of a vector potential, $\bar{\psi}$, i.e.,

$$\bar{u} = \nabla \phi + \nabla \times \bar{\psi}. \quad (7)$$

In spherical coordinates for axisymmetric motion the components of \bar{u} from Eq. (7) are found to be

$$w = \left[\frac{\partial \phi}{\partial r} + \frac{1}{r \sin \phi} \frac{\partial}{\partial \phi} (\psi \sin \phi) \right] \quad \left. \begin{array}{l} \text{where } \psi \text{ is the component of } \bar{\psi} \\ \text{along } \theta\text{-direction} \end{array} \right\} \quad (8)$$

$$u = \left[\frac{1}{r} \frac{\partial \phi}{\partial \phi} - \frac{1}{r} \frac{\partial}{\partial r} (\psi r) \right] \quad (9)$$

Since the excitation is harmonic and applied locally on the spherical surface, the following expansions are considered for ϕ and ψ :

$$\phi = \sum_{n=0}^{\infty} \phi_n(r) P_n(\cos \phi) e^{i\omega t} \quad (10)$$

$$\psi = \sum_{n=1}^{\infty} \psi_n(r) P_n'(\cos \phi) e^{i\omega t} \quad (11)$$

where $P_n(\cos \phi)$ are Legendre polynomials of the first order, first kind. In view of the fact that the second solutions of the Legendre equations are singular at the poles they are not included in the expansions (10) and (11). In Eqs. (10) and (11) ω and t are the frequency of harmonic excitation and time respectively. Next, let us substitute Eqs. (10) and (11) into Eqs. (8) and (9) and defining $dP_n/d\phi \equiv \dot{P}_n$, etc. and with the relation $P_n'(\cos \phi) = \dot{P}_n(\cos \phi)$ we obtain the following

$$w = \left\{ \frac{d\phi_0}{dr} + \sum_{n=1}^{\infty} \left[\frac{d\phi_n}{dr} P_n + \frac{\psi_n}{r} (\cot\phi \dot{P}_n + \ddot{P}_n) \right] \right\} e^{i\omega t} \quad (12)$$

$$u = \frac{1}{r} \left\{ \sum_{n=1}^{\infty} \left(\phi_n - \psi_n - r \frac{d\psi_n}{dr} \right) \dot{P}_n \right\} e^{i\omega t} \quad (13)$$

For brevity the arguments of the Legendre polynomials in Eqs. (12), (13) and in the subsequent equations are not shown. The equations of motion (3) and (4) contain terms like Δ , cubical dilatation, and ω_θ . We evaluate these by substituting the expressions of displacement components, Eqs. (12) and (13), into Eqs. (5) and (6). The resulting equations are

$$\Delta = \left\{ \frac{d^2\phi_0}{dr^2} + \frac{2}{r} \frac{d\phi_0}{dr} + \sum_{n=1}^{\infty} \left[\left(\frac{d^2\phi_n}{dr^2} + \frac{2}{r} \frac{d\phi_n}{dr} \right) P_n + (\cot\phi \dot{P}_n + \ddot{P}_n) \frac{\phi_n}{r^2} \right] \right\} e^{i\omega t} \quad (14)$$

$$\omega_\theta = \frac{1}{2r^2} \left\{ \sum_{n=1}^{\infty} \left[\left(\frac{\psi_n}{\sin^2\phi} - 2r \frac{d\psi_n}{dr} - r^2 \frac{d^2\psi_n}{dr^2} \right) \dot{P}_n - \psi_n (\cot\phi \ddot{P}_n + \ddot{P}_n) \right] \right\} e^{i\omega t} \quad (15)$$

Here we make a note that the Legendre polynomials satisfy the following differential equation

$$\ddot{P}_n + \dot{P}_n \cot\phi + \lambda_n P_n = 0 \quad (16)$$

where $\lambda_n = n(n+1)$.

Substitution of Eqs. (12) - (15) into the first of the equations of motion, namely, Eq. (3) and repeated use of Eq. (16) in various places, after rather lengthy manipulation, yields the following expression

$$\begin{aligned}
& (\lambda + 2G) \frac{d}{dr} \left\{ \sum_{n=0}^{\infty} \left[\frac{d^2 \phi_n}{dr^2} + \frac{2}{r} \frac{d\phi_n}{dr} - \frac{\lambda_n}{r^2} \phi_n \right] P_n \right\} - \frac{G}{r} \left\{ \sum_{n=1}^{\infty} \left[\frac{d^2 \psi_n}{dr^2} + \right. \right. \\
& \left. \left. \frac{2}{r} \frac{d\psi_n}{dr} - \frac{\lambda_n}{r^2} \psi_n \right] \lambda_n P_n \right\} = -\rho\omega^2 \sum_{n=0}^{\infty} \left[\frac{d\phi_n}{dr} - \frac{\psi_n}{r} \lambda_n \right] P_n
\end{aligned} \tag{17}$$

Similarly the second equation of motion, Eq. (4), can be expressed as

$$\begin{aligned}
& (\lambda + 2G) \frac{1}{r} \sum_{n=0}^{\infty} \left[\frac{d^2 \phi_n}{dr^2} + \frac{2}{r} \frac{d\phi_n}{dr} - \frac{\lambda_n}{r^2} \phi_n \right] \dot{P}_n - \frac{G}{r} \left\{ \sum_{n=1}^{\infty} \left[\frac{d^2 \psi_n}{dr^2} + \right. \right. \\
& \left. \left. \frac{2}{r} \frac{d\psi_n}{dr} - \frac{\lambda_n}{r^2} \psi_n \right] \dot{P}_n + r \frac{d}{dr} \sum_{n=1}^{\infty} \left[\frac{d^2 \psi_n}{dr^2} + \frac{2}{r^2} \frac{d\psi_n}{dr} - \frac{\lambda_n}{r} \psi_n \right] \dot{P}_n \right\} = \\
& -\rho\omega^2 \sum_{n=1}^{\infty} \left[\frac{\phi_n}{r} - \frac{\psi_n}{r} - \frac{d\psi_n}{dr} \right] \dot{P}_n
\end{aligned} \tag{18}$$

One can easily see that Eq. (17) is satisfied if the solutions of the following differential equations are found

$$\text{i) } \frac{d^2 \phi_n}{dr^2} + \frac{2}{r} \frac{d\phi_n}{dr} - \frac{\lambda_n}{r^2} \phi_n = \frac{-\rho\omega^2}{\lambda + 2G} \phi_n \quad n = 0, 1, 2, \dots \tag{19}$$

$$\text{ii) } \frac{d^2 \psi_n}{dr^2} + \frac{2}{r} \frac{d\psi_n}{dr} - \frac{\lambda_n}{r^2} \psi_n = \frac{-\rho\omega^2}{G} \psi_n \quad n = 1, 2, 3, \dots \tag{20}$$

The solutions of these two equations also satisfy Eq. (18). Thus, we can state that equations (19) and (20) are the two sets of differential equations that have to be solved.

Eqs. (19) and (20) can also be rewritten as

$$r^2 \frac{d^2 \phi_n}{dr^2} + 2r \frac{d\phi_n}{dr} + (k_1^2 r^2 - \lambda_n) \phi_n = 0 \quad n = 0, 1, 2, \dots \quad (21)$$

$$r^2 \frac{d^2 \psi_n}{dr^2} + 2r \frac{d\psi_n}{dr} + (k_2^2 r^2 - \lambda_n) \psi_n = 0 \quad n = 1, 2, 3, \dots \quad (22)$$

where

$$k_1^2 = \frac{\rho\omega^2}{\lambda+2G} \quad \text{and} \quad k_2^2 = \frac{\rho\omega^2}{G}$$

The finite solutions of the above differential equations are the spherical Bessel function of the first kind

$$\phi_n = a_n j_n(k_1 r) \quad n = 0, 1, 2, \dots$$

$$\psi_n = b_n j_n(k_2 r) \quad n = 1, 2, 3, \dots$$

where $j_n(k_1 r)$ and $j_n(k_2 r)$ are the spherical Bessel functions with arguments $k_1 r$ and $k_2 r$ respectively; a_n and b_n are the constants to be determined later.

Substitution of the solutions ϕ_n and ψ_n into Eqs. (10) - (13) yields

$$\begin{aligned} \phi &= \sum_{n=0}^{\infty} a_n j_n(k_1 r) P_n e^{i\omega t} \\ \psi &= \sum_{n=1}^{\infty} b_n j_n(k_2 r) P_n e^{i\omega t} \\ w &= \left\{ a_0 k_1 j_0'(k_1 r) + \sum_{n=1}^{\infty} [a_n k_1 j_n'(k_1 r) - \frac{\lambda_n}{r} b_n j_n(k_2 r)] P_n \right\} e^{i\omega t} \\ u &= \left\{ \frac{1}{r} \sum_{n=1}^{\infty} [a_n j_n(k_1 r) - b_n j_n(k_2 r) - r b_n k_2 j_n'(k_2 r)] P_n \right\} e^{i\omega t} \end{aligned} \quad (23)$$

where (') denotes differentiation with respect to argument.

The coefficients a_n and b_n are determined by utilizing the following appropriate boundary conditions

- i) Vanishing of the shear stress at the interface of elastic (or viscoelastic) material and the rigid boundary, i.e. $\tau_{r\phi}(a, \phi) = 0$
- ii) Local application of the radial displacement, i.e.

$$w(a, \phi) = W(\phi)e^{i\omega t}, \text{ in particular, } W(\phi) = \begin{cases} W_0 & 0 \leq \phi \leq \phi_0 \\ 0 & \phi_0 < \phi \leq \pi \end{cases}$$

where W_0 is the maximum amplitude of excitation.

From the first boundary condition we obtain

$$\left(\frac{1}{r} \frac{\partial w}{\partial \phi} - \frac{u}{r} + \frac{\partial u}{\partial r} \right) \Big|_{r=a} = 0 \quad (24)$$

Substitution of displacement components from Eq. (23) into Eq. (24) yields

$$\sum_{n=1}^{\infty} \left\{ 2a_n \left[k_1 j_n'(k_1 a) - \frac{j_n(k_1 a)}{a} \right] - b_n \left[(\lambda_n - 2) \frac{j_n(k_2 a)}{a} + k_2^2 a j_n''(k_2 a) \right] \right\} P_n = 0$$

$$\text{for each } n \geq 1 \quad b_n = \frac{2 \left[k_1 j_n'(k_1 a) - \frac{j_n(k_1 a)}{a} \right]}{\frac{(\lambda_n - 2) j_n(k_2 a)}{a} + k_2^2 a j_n''(k_2 a)} a_n \quad (25)$$

The second boundary condition in the view of Eq. (23) give the following relation

$$a_0 k_1 j_0'(k_1 a) + \sum_{n=1}^{\infty} \left[a_n k_1 j_n'(k_1 a) - \frac{\lambda_n}{a} b_n j_n(k_2 a) \right] P_n = W(\phi) \quad (26)$$

Before proceeding further we expand the function $W(\phi)$ in a series of Legendre polynomials of the form

$$W(\phi) = \sum_{n=0}^{\infty} c_n P_n(\cos \phi) \quad (27)$$

where the coefficients c_n are found, by the usual methods, to be

$$c_n = \frac{1}{2} W_0 [P_{n-1}(\cos\phi_0) - P_{n+1}(\cos\phi_0)] \quad n = 0, 1, 2, \dots$$

it being realized, of course, that $P_{-1}(\cos\phi_0) \equiv 1$. (28)

Substituting Eqs. (25) and (27) into Eq. (26) yields

$$\begin{aligned} a_0 k_1 j_0'(k_1 a) + \sum_{n=1}^{\infty} a_n \left\{ k_1 j_n'(k_1 a) - \frac{2\lambda_n [k_1 a j_n'(k_1 a) - j_n(k_1 a)] j_n(k_2 a)}{(\lambda_n - 2) j_n(k_2 a) + k_2^2 a^2 j_n''(k_2 a)} \right\} P_n(\cos\phi) \\ = \sum_{n=0}^{\infty} c_n P_n(\cos\phi) \end{aligned}$$

Comparison of coefficients in the previous equation give the following

$$\text{for } n = 0 \quad a_0 = \frac{c_0}{k_1 j_0'(k_1 a)} \quad \text{and for } n \geq 1 \quad (29)$$

$$a_n = \frac{a [(\lambda_n - 2) j_n(k_2 a) + k_2^2 a^2 j_n''(k_2 a)] c_n}{k_1 a j_n'(k_1 a) [(\lambda_n - 2) j_n(k_2 a) + k_2^2 a^2 j_n''(k_2 a)] - 2\lambda_n [k_1 a j_n'(k_1 a) - j_n(k_1 a)] j_n(k_2 a)} \quad (30)$$

also from Eqs. (25) and (30) for $n \geq 1$

$$b_n = \frac{2a [k_1 a j_n'(k_1 a) - j_n(k_1 a)] c_n}{k_1 a j_n'(k_1 a) [(\lambda_n - 2) j_n(k_2 a) + k_2^2 a^2 j_n''(k_2 a)] - 2\lambda_n [k_1 a j_n'(k_1 a) - j_n(k_1 a)] j_n(k_2 a)} \quad (31)$$

Here we note that second derivative of spherical Bessel function appearing in Eqs. (30) and (31) can be eliminated by utilization of the differential equation whose solutions are the spherical Bessel functions.

Having determined the coefficients a_n and b_n we can now obtain displacement components w and u from Eq. (23). For an isotropic elastic material, the stress, σ_{ij} , and strain, ϵ_{ij} , tensors are related in a following manner

$$\sigma_{ij} = \lambda \Delta \delta_{ij} + 2G \epsilon_{ij}, \quad \delta_{ij} \begin{cases} = 1 & \text{for } i = j \\ = 0 & \text{for } i \neq j \end{cases} \quad (32)$$

where $\lambda = \frac{G(E-2G)}{3G-E}$, E and G are modulus of elasticity and shear modulus respectively. Substituting Eq. (23) into Eq. (5) yields the cubical dilatation, Δ , for the axisymmetric motion of the material

$$\Delta = -k_1^2 \sum_{n=0}^{\infty} a_n j_n(k_1 r) P_n(\cos \phi) e^{i\omega t} \quad (33)$$

Since we are interested in the normal stress in the radial direction ϵ_{rr} is obtained from

$$\epsilon_{rr} = \frac{\partial w}{\partial r} = \left\{ \sum_{n=0}^{\infty} a_n \left[-\frac{2k_1}{r} j_n'(k_1 r) - k_1^2 \left(1 - \frac{\lambda_n}{k_1^2 r^2} \right) j_n(k_1 r) \right] P_n(\cos \phi) + \sum_{n=1}^{\infty} \lambda_n b_n \left[\frac{j_n(k_2 r)}{r^2} - \frac{k_2 j_n'(k_2 r)}{r} \right] P_n(\cos \phi) \right\} e^{i\omega t} \quad (34)$$

Thus, from Eqs. (32) and (34) the final form of the normal stress, σ_{rr} , is

$$\begin{aligned} \sigma_{rr} = & \sum_{n=0}^{\infty} a_n \left\{ -\lambda k_1^2 j_n(k_1 r) - 2G \left[\frac{2k_1}{r} j_n'(k_1 r) - k_1^2 \left(1 - \frac{\lambda_n}{k_1^2 r^2} \right) j_n(k_1 r) \right] \right\} P_n(\cos \phi) e^{i\omega t} \\ & + 2G \sum_{n=1}^{\infty} \lambda_n b_n \left[\frac{j_n(k_2 r)}{r^2} - \frac{k_2 j_n'(k_2 r)}{r} \right] P_n(\cos \phi) e^{i\omega t} \end{aligned} \quad (35)$$

This completes the elastic solution.

b) Viscoelastic Response The elastic solutions obtained in the part (a) can be converted to viscoelastic response solutions through the use of the elastic-viscoelastic correspondence principle applicable to steady state oscillations as discussed by Bland (1960). According to this principle the two independent elastic constants such as the elastic shear modulus, G , and the modulus of elasticity, E , are replaced by the complex shear modulus $G^* = G' + iG''$ and complex modulus of elasticity, $E^* = E' + iE''$ respectively. Both real and imaginary parts of G^* and E^* are, in general, functions of frequency.

Since G and E are replaced by G^* and E^* , k_1 , k_2 and λ should be replaced by k_1^* , k_2^* and λ^* . They are defined to be

$$\begin{aligned} \lambda^* &= \frac{G^*(E^* - 2G^*)}{3G^* - E^*} \\ k_1^* &= \left(\frac{\rho\omega^2}{\lambda^* + 2G^*} \right)^{1/2} \\ k_2^* &= \left(\frac{\rho\omega^2}{G^*} \right)^{1/2} \end{aligned} \quad (36)$$

The coefficients a_n and b_n which were defined in the preceding sections now become complex functions, a_n^* and b_n^* , of k_1^* , k_2^* and spherical Bessel functions of complex arguments. In view of this the normal stress, σ_{rr} , will take the following form

$$\begin{aligned} \sigma_{rr} = & \sum_{n=0}^{\infty} a_n^* \left\{ -\lambda^* k_1^* j_n(k_1^* r) - 2G^* \left[\frac{2k_1^*}{r} j_n'(k_1^* r) + k_1^* \left(1 - \frac{\lambda_n}{k_1^* r^2} \right) j_n(k_1^* r) \right] \right\} P_n(\cos \phi) e^{i\omega t} \\ & + 2G^* \sum_{n=0}^{\infty} \lambda_n b_n^* \left[\frac{j_n(k_2^* r)}{r^2} - \frac{k_2^* j_n'(k_2^* r)}{r} \right] P_n(\cos \phi) e^{i\omega t} \end{aligned} \quad (37)$$

The procedure of separating the complex stress, σ_{rr} , into the real and imaginary parts are shown, in some detail, in the appendix. Having performed this we obtain the following expression for the radial normal stress

$$\begin{aligned} \sigma_{rr}(r, \phi, t) &= \sum_{n=0}^{\infty} [Z_{n1}(r) + iZ_{n2}(r)] P_n(\cos \phi) e^{i\omega t} \\ &= [Z_1(r, \phi) + iZ_2(r, \phi)] e^{i\omega t} \\ &= \left| \sigma_{rr} \right| e^{i(\omega t + \delta)} \end{aligned} \quad (38)$$

$$\text{where } Z_1(r, \phi) = \sum_{n=0}^{\infty} Z_{n1}(r) P_n(\cos \phi)$$

$$Z_2(r, \phi) = \sum_{n=0}^{\infty} Z_{n2}(r) P_n(\cos \phi)$$

$$\left| \sigma_{rr} \right| = [Z_1^2(r, \phi) + Z_2^2(r, \phi)]^{1/2}$$

$$\delta = \tan^{-1} \frac{Z_2(r, \phi)}{Z_1(r, \phi)}$$

The definitions of Z_{n1} and Z_{n2} are given in the appendix. In Eq. (38) δ is the phase angle between the variation of stress and the variation of strain.

The radial normal force under the probe is given by

$$F_r = \int_0^{\phi_0} \sigma_{rr}(a, \phi, t) dA$$

where $dA = 2\pi a^2 \sin\phi d\phi$. In view of Eq. (38) above integral can be written as

$$F_r = 2\pi a^2 \int_0^{\phi_0} [Z_1(a, \phi) + iZ_2(a, \phi)] \sin\phi d\phi e^{i\omega t} \quad (39)$$

DISCUSSION

As shown schematically in Fig. 1 the apparatus has an acceleration transducer 1 and force transducer 2 which measures a composite signal consisting of the force caused by the acceleration of the probe mass and the force transferred to the test object. By a proper calibration of these two transducers one can obtain the shape and magnitudes of force and displacement quantities. A typical test supplies two sets of information; namely, phase relations between the force and displacement and the magnitude of force. Since the brain is essentially incompressible we can assume that the viscoelastic material contained in the rigid spherical shell is incompressible. For an incompressible viscoelastic material $3G^* = E^*$, thus the knowledge of the two material constants (or functions if one seeks frequency dependent relations) is sufficient. Let us consider to choose G' and G'' to be determined from a combined relationship of theoretical analysis and experimental data. For this task we carry on the following steps:

- a) From Eq. 39 obtain the numerical value of the complex force that the material exerts on the probe. For a viscoelastic material, mathematical analysis will give a complex force, real part of which is in phase with displacement and the imaginary part 90° out of phase. Hence, the ratio of the imaginary part of the force to the real part will be the tangent of the phase angle between displacement and force.
- b) Plot the theoretically obtained phase angles versus G' for various values of G'' . Here, we make the remark that the values of G' and G'' can be initially chosen arbitrarily. This plot is in the form of family of curves. On this plot draw a line passing through the experimental

value of the phase angle and parallel to G' axis. This line will be intersecting the family of curves at various points which define pairs of values for G' and G'' .

- c) Using these pairs of G' and G'' obtain the numerical values of theoretical force and plot these force values versus G' . This plot will be only a single curve. The value of the experimental force determines a point on this curve. G' and G'' defined by this point are the proper material constants for the corresponding frequency.

Utilizing the method outlined above one can obtain the real and imaginary parts of G^* for various frequencies. The knowledge of G^* are a function of frequency is very essential for the construction of transient response of the viscoelastic material.

ACKNOWLEDGEMENT

This work was supported by National Institute for Neurological Diseases and Blindness Contract No. PH-43-67-1136.

REFERENCES

- Anzelius, A. (1943) The effect of an impact on a spherical liquid mass
Acta. Path. Microbiol. Scand. Supp. 48
- Bland, D. R. (1960) The Theory of Linear Viscoelasticity, p. 67 Pergamon Press
- Dodgson, M. C. H. (1962) Colloidal structure of brain, Biorheology, Vol. 1 pp. 21-30
- Engin, A. E. (1969) The axysmmetric response of a fluid-filled spherical shell to a local radial impulse -- a model for head injury
Journal of Biomechanics Vol. 2, 3, pp. 325-341.
- Fallenstein, G. T., Hulce, V. D., Melvin, J. W. (1969) Dynamic mechanical properties of human brain tissue, Journal of Biomechanics Vol. 2, 3 pp. 217-226.
- Franke, E. K. (1954) The response of the human skull to mechanical vibrations, Wright-Patterson Air Force Base, Ohio, WADC Tech. Rept. pp. 24-54
- Fung, Y. C. (1965) Foundations of Solid Mechanics, pp. 154-156, Prentice-Hall, Inc. Englewood Cliffs, New Jersey
- Güttinger, W. (1950) Der Stosseffekt auf eine Flüssigkeitskugel als Grundlage einer Physikalischen Theorie der Entstehung von Gehirnverletzungen.
Zeit. f. Naturf. A5, pp. 622-628
- Holbourn, A. H. S. (1943) Mechanics of Head Injury Lancet, Vol. 2, pp. 438-441
- Koeneman, J. B. (1966) Viscoelastic properties of brain tissue, M.S. Thesis, Case Institute of Technology

APPENDIX

For the viscoelastic material the complex moduli are defined to be

$$\begin{aligned} G^* &= G' + iG'' \\ E^* &= E' + iE'' \end{aligned} \quad (I)$$

Also Lamé's constant, λ , in viscoelastic case takes the form of

$$\lambda^* = \frac{G^*(E^* - 2G^*)}{3G^* - E^*} \quad (II)$$

Substitution of (I) into (II) and rationalizing the resulting equation gives

$$\lambda^* = \text{Re}(\lambda^*) + i\text{Im}(\lambda^*) \quad (III)$$

where

$$\text{Re}(\lambda^*) = \frac{[G'(E' - 2G') - G''(E'' - 2G'')](3G' - E') + [G''(E' - 2G') + G'(E'' - 2G'')](3G'' - E'')}{(3G' - E')^2 + (3G'' - E'')^2}$$

$$\text{Im}(\lambda^*) = \frac{[G''(E' - 2G') + G'(E'' - 2G'')](3G' - E') - [G'(E' - 2G') - G''(E'' - 2G'')](3G'' - E'')}{(3G' - E')^2 + (3G'' - E'')^2}$$

Note that $\text{Re}(\)$ and $\text{Im}(\)$ denote the real and the imaginary parts of the complex function inside of the paranthesis respectively.

The arguments of the spherical Bessel functions contain k_1 and k_2 which involve λ^* and G^* ; hence k_1 and k_2 become complex and they are

$$\begin{aligned} k_1^* &= \left(\frac{\rho\omega^2}{\lambda^* + 2G^*} \right)^{1/2} & \text{and} & & k_2^* &= \left(\frac{\rho\omega^2}{G^*} \right)^{1/2} \\ &= \text{Re}(k_1^*) + i\text{Im}(k_1^*) & & & &= \text{Re}(k_2^*) + i\text{Im}(k_2^*) \end{aligned} \quad (IV)$$

where

$$\text{Re}(k_1^*) = \frac{\omega\rho^{1/2} \left\{ [(\text{Re}(\lambda^*) + 2G')^2 + (\text{Im}(\lambda^*) + 2G'')^2]^{1/2} + \text{Re}(\lambda^*) + 2G' \right\}^{1/2}}{[2(\text{Re}(\lambda^*) + 2G')^2 + 2(\text{Im}(\lambda^*) + 2G'')^2]^{1/2}}$$

$$\begin{aligned} \text{Im}(k_1^*) &= \frac{\omega_p^{1/2} \left\{ [(\text{Re}(\lambda^*) + 2G')^2 + (\text{Im}(\lambda^*) + 2G'')^2]^{1/2} - \text{Re}(\lambda^*) - 2G' \right\}^{1/2}}{[2(\text{Re}(\lambda^*) + 2G')^2 + 2(\text{Im}(\lambda^*) + 2G'')^2]^{1/2}} \\ \text{Re}(k_2^*) &= \frac{\omega_p^{1/2} [(G'^2 + G''^2)^{1/2} + G']^{1/2}}{[2G'^2 + 2G''^2]^{1/2}} \\ \text{Im}(k_2^*) &= \frac{\omega_p^{1/2} [(G'^2 + G''^2)^{1/2} - G']^{1/2}}{[2G'^2 + 2G''^2]^{1/2}} \end{aligned} \quad (V)$$

To obtain (V) the following relation has been used

$$(x \pm iy)^{1/2} = \left(\frac{r+x}{2}\right)^{1/2} \pm \left(\frac{r-x}{2}\right)^{1/2}$$

where

$$r = (x^2 + y^2)^{1/2}$$

For the viscoelastic material the relationship between a_n and b_n becomes complex in the following manner

$$b_n^* = \frac{2k_1^* j_n(k_1^* a) - \frac{2j_n(k_1^* a)}{a}}{\frac{(\lambda_n - 2)}{a} j_n(k_2^* a) + k_2^{*2} a j_n''(k_2^* a)} a_n^* \quad (VI)$$

let

$$X_n = 2 \left[k_1^* j_n'(k_1^* a) - \frac{j_n(k_1^* a)}{a} \right]$$

$$= \text{Re}(X_n) + i \text{Im}(X_n)$$

$$Y_n = \frac{\lambda_n - 2}{a} j_n(k_2^* a) + k_2^{*2} a j_n''(k_2^* a)$$

$$= \text{Re}(Y_n) + i \text{Im}(Y_n)$$

where

$$\operatorname{Re}(X_n) = 2\operatorname{Re}(k_1^*)\operatorname{Re}[j_n'(k_1^*a)] - 2\operatorname{Im}(k_1^*)\operatorname{Im}[j_n'(k_1^*a)] - 2\operatorname{Re}[j_n(k_1^*a)]/a$$

$$\operatorname{Im}(X_n) = 2\operatorname{Im}(k_1^*)\operatorname{Re}[j_n'(k_1^*a)] + 2\operatorname{Re}(k_1^*)\operatorname{Im}[j_n'(k_1^*a)] - 2\operatorname{Im}[j_n(k_1^*a)]/a$$

$$\begin{aligned} \operatorname{Re}(Y_n) = & \left[\frac{2(\lambda_n - 1)}{a} - a\operatorname{Re}(k_2^{*2}) \right] \operatorname{Re}[j_n(k_2^*a)] + a\operatorname{Im}(k_2^{*2})\operatorname{Im}[j_n(k_2^*a)] \\ & - 2\operatorname{Re}(k_2^*)\operatorname{Re}[j_n'(k_2^*a)] - 2\operatorname{Im}(k_2^*)\operatorname{Im}[j_n'(k_2^*a)] \end{aligned}$$

$$\begin{aligned} \operatorname{Im}(Y_n) = & \left[\frac{2(\lambda_n - 1)}{a} - a\operatorname{Re}(k_2^{*2}) \right] \operatorname{Im}[j_n(k_2^*a)] - a\operatorname{Im}(k_2^{*2})\operatorname{Re}[j_n(k_2^*a)] \\ & - 2\operatorname{Im}(k_2^*)\operatorname{Re}[j_n'(k_2^*a)] + 2\operatorname{Re}(k_2^*)\operatorname{Im}[j_n'(k_2^*a)] \end{aligned}$$

Now (VI) can be written as

$$b_n^* = \frac{\operatorname{Re}(X_n) + i\operatorname{Im}(X_n)}{\operatorname{Re}(Y_n) + i\operatorname{Im}(Y_n)} a_n^* = \left[\operatorname{Re}\left(\frac{X_n}{Y_n}\right) + i\operatorname{Im}\left(\frac{X_n}{Y_n}\right) \right] a_n^* \quad (\text{VII})$$

where

$$\operatorname{Re}\left(\frac{X_n}{Y_n}\right) = \frac{\operatorname{Re}(X_n)\operatorname{Re}(Y_n) + \operatorname{Im}(X_n)\operatorname{Im}(Y_n)}{[\operatorname{Re}(Y_n)]^2 + [\operatorname{Im}(Y_n)]^2}$$

$$\operatorname{Im}\left(\frac{X_n}{Y_n}\right) = \frac{\operatorname{Im}(X_n)\operatorname{Re}(Y_n) - \operatorname{Re}(X_n)\operatorname{Im}(Y_n)}{[\operatorname{Re}(Y_n)]^2 + [\operatorname{Im}(Y_n)]^2}$$

From Eq. (26)

$$a_0^* k_1^* j_0'(k_1^*a) + \sum_{n=1}^{\infty} [a_n^* k_1^* j_n'(k_1^*a) - \frac{\lambda_n}{a} b_n^* j_n(k_2^*a)] P_n = \sum_{n=0}^{\infty} c_n P_n$$

$$a_0^* = \frac{c_0}{k_1^* j_0'(k_1^*a)} \quad \text{and} \quad a_n^* = \frac{c_n}{[k_1^* j_n'(k_1^*a) - \frac{\lambda_n}{a} \frac{X_n}{Y_n} j_n(k_2^*a)]} \quad n = 1, 2, 3, \dots$$

or

$$a_n^* = \frac{c_n}{[A_r - \operatorname{Re}\left(\frac{X_n}{Y_n} j_n\right)] + i[A_i - \operatorname{Im}\left(\frac{X_n}{Y_n} j_n\right)]} \quad n = 1, 2, 3, \dots \quad (\text{VIII})$$

where $A_r = \operatorname{Re}(k_1^*)\operatorname{Re}[j_n'(k_1^*a)] - \operatorname{Im}(k_1^*)\operatorname{Im}[j_n'(k_1^*a)]$

$$A_i = \text{Im}(k_i^*) \text{Re}[j_n'(k_i^* a)] + \text{Re}(k_i^*) \text{Im}[j_n'(k_i^* a)]$$

$$\text{Re}\left(\frac{\lambda_n}{Y_n} j_n\right) = \frac{\lambda_n}{a} \left\{ \text{Re}\left(\frac{\lambda_n}{Y_n}\right) \text{Re}[j_n(k_2^* a)] - \text{Im}\left(\frac{\lambda_n}{Y_n}\right) \text{Im}[j_n(k_2^* a)] \right\}$$

$$\text{Im}\left(\frac{\lambda_n}{Y_n} j_n\right) = \frac{\lambda_n}{a} \left\{ \text{Im}\left(\frac{\lambda_n}{Y_n}\right) \text{Re}[j_n(k_2^* a)] + \text{Re}\left(\frac{\lambda_n}{Y_n}\right) \text{Im}[j_n(k_2^* a)] \right\}$$

Eq. (VIII) now becomes

$$a_n^* = \text{Re}(a_n^*) + i \text{Im}(a_n^*) \quad n = 1, 2, 3, \dots \quad (\text{IX})$$

where

$$\text{Re}(a_n^*) = \frac{c_n [A_r - \text{Re}\left(\frac{\lambda_n}{Y_n} j_n\right)]}{[A_r - \text{Re}\left(\frac{\lambda_n}{Y_n} j_n\right)]^2 + [A_i - \text{Im}\left(\frac{\lambda_n}{Y_n} j_n\right)]^2}$$

$$\text{Im}(a_n^*) = \frac{-c_n [A_i - \text{Im}\left(\frac{\lambda_n}{Y_n} j_n\right)]}{[A_r - \text{Re}\left(\frac{\lambda_n}{Y_n} j_n\right)]^2 + [A_i - \text{Im}\left(\frac{\lambda_n}{Y_n} j_n\right)]^2}$$

Substituting Eq. (IX) into Eq. (VII) we get

$$b_n^* = \text{Re}(b_n^*) + i \text{Im}(b_n^*)$$

where

$$\text{Re}(b_n^*) = \text{Re}\left(\frac{\lambda_n}{Y_n}\right) \text{Re}(a_n^*) - \text{Im}\left(\frac{\lambda_n}{Y_n}\right) \text{Im}(a_n^*)$$

$$\text{Im}(b_n^*) = \text{Re}\left(\frac{\lambda_n}{Y_n}\right) \text{Im}(a_n^*) + \text{Im}\left(\frac{\lambda_n}{Y_n}\right) \text{Re}(a_n^*)$$

Putting all the above Eqs. (I) - (IX) into the Eq. (37) we get the following expressions for the complex normal stress

$$\begin{aligned}
\sigma_{rr} = & \sum_{n=0}^{\infty} a_n^* \left\langle -[\operatorname{Re}(\lambda^*) + i\operatorname{Im}(\lambda^*)][\operatorname{Re}(k_1^*{}^2) + i\operatorname{Im}(k_1^*{}^2)] \left\{ \operatorname{Re}[j_n(k_1^*r)] \right. \right. \\
& + i\operatorname{Im}[j_n(k_1^*r)] \left. \right\} - \frac{4}{r}(G' + iG'')[\operatorname{Re}(k_1^*) + i\operatorname{Im}(k_1^*)] \left\{ \operatorname{Re}[j_n'(k_1^*r)] \right. \\
& + i\operatorname{Im}[j_n'(k_1^*r)] \left. \right\} - 2(G' + iG'')[\operatorname{Re}(k_1^*{}^2) + i\operatorname{Im}(k_1^*{}^2)] \left\{ \operatorname{Re}[j_n(k_1^*r)] \right. \\
& + i\operatorname{Im}[j_n(k_1^*r)] \left. \right\} \cdot \left. \left\{ 1 - \frac{\lambda_n}{[\operatorname{Re}(k_1^*{}^2) - i\operatorname{Im}(k_1^*{}^2)]r^2} \right\} \right\rangle P_n(\cos\phi)e^{i\omega t} \\
& + \sum_{n=0}^{\infty} 2\lambda_n(G' + iG'') \cdot [\operatorname{Re}(b_n^*) + i\operatorname{Im}(b_n^*)] \left\langle \frac{\operatorname{Re}[j_n(k_2^*r)] + i\operatorname{Im}[j_n(k_2^*r)]}{r^2} \right. \\
& - \frac{[\operatorname{Re}(k_2^*) + i\operatorname{Im}(k_2^*)]}{r} \left. \left\{ \operatorname{Re}[j_n'(k_2^*r)] + i\operatorname{Im}[j_n'(k_2^*r)] \right\} \right\rangle P_n(\cos\phi)e^{i\omega t}
\end{aligned} \tag{X}$$

Next, let us define the following expressions:

$$\begin{aligned}
q_1 &= \operatorname{Re}(\lambda^*)\operatorname{Re}(k_1^*{}^2) - \operatorname{Im}(\lambda^*)\operatorname{Im}(k_1^*{}^2) \\
q_2 &= \operatorname{Re}(\lambda^*)\operatorname{Im}(k_1^*{}^2) + \operatorname{Im}(\lambda^*)\operatorname{Re}(k_1^*{}^2) \\
q_3 &= G'\operatorname{Re}(k_1^*) - G''\operatorname{Im}(k_1^*) \\
q_4 &= G'\operatorname{Im}(k_1^*) + G''\operatorname{Re}(k_1^*) \\
q_5 &= G'\operatorname{Re}(k_1^*{}^2) - G''\operatorname{Im}(k_1^*{}^2) \\
q_6 &= G'\operatorname{Im}(k_1^*{}^2) + G''\operatorname{Re}(k_1^*{}^2) \\
q_7 &= \left\{ [\operatorname{Re}(k_1^*{}^2)]^2 + [\operatorname{Im}(k_1^*{}^2)]^2 \right\} r^2 \\
q_8 &= G'\operatorname{Re}(b_n^*) - G''\operatorname{Im}(b_n^*)
\end{aligned} \tag{XI}$$

$$q_9 = G' \text{Im}(b_n^*) + G'' \text{Re}(b_n^*)$$

$$q_{10} = \text{Re}(k_2^*) \text{Re}[j_n'(k_2^* r)] - \text{Im}(k_2^*) \text{Im}[j_n'(k_2^* r)]$$

$$q_{11} = \text{Re}(k_2^*) \text{Im}[j_n'(k_2^* r)] + \text{Im}(k_2^*) \text{Re}[j_n'(k_2^* r)]$$

Eq. (X) in view of expressions defined by Eq. (XI) can be written as

$$\begin{aligned} \sigma_{rr} = & \sum_{n=0}^{\infty} [\text{Re}(a_n^*) + i \text{Im}(a_n^*)] \left\langle - \left\{ q_1 \text{Re}[j_n(k_1^* r)] - q_2 \text{Im}[j_n(k_1^* r)] + \right. \right. \\ & \left. \left. i q_1 \text{Im}[j_n(k_1^* r)] + i q_2 \text{Re}[j_n(k_1^* r)] \right\} - \frac{4}{r} \left\{ q_3 \text{Re}[j_n'(k_1^* r)] - q_4 \text{Im}[j_n'(k_1^* r)] \right. \right. \\ & \left. \left. + i q_3 \text{Im}[j_n'(k_1^* r)] + i q_4 \text{Re}[j_n'(k_1^* r)] \right\} - 2(q_5 + i q_6) \left\{ \frac{[q_7 - \lambda_n \text{Re}(k_1^{*2})] \text{Re}[j_n(k_1^* r)]}{q_7} \right. \right. \\ & \left. \left. - \frac{\lambda_n \text{Im}(k_1^{*2}) \text{Im}[j_n(k_1^* r)]}{q_7} + i \frac{[q_7 - \lambda_n \text{Re}(k_1^{*2})] \text{Im}[j_n(k_1^* r)]}{q_7} \right. \right. \\ & \left. \left. + i \frac{\lambda_n \text{Im}(k_1^{*2}) \text{Re}[j_n(k_1^* r)]}{q_7} \right\} \right\rangle \cdot P_n(\cos \phi) e^{i\omega t} + \sum_{n=0}^{\infty} 2\lambda_n \\ & \cdot \left\langle \left\{ q_8 \frac{\text{Re}[j_n(k_2^* r)] - r q_{10}}{r^2} - q_9 \frac{\text{Im}[j_n(k_2^* r)] - r q_{11}}{r^2} \right\} \right. \\ & \left. + i \left\{ q_8 \frac{\text{Im}[j_n(k_2^* r)] - r q_{11}}{r^2} + q_9 \frac{\text{Re}[j_n(k_2^* r)] - r q_{10}}{r^2} \right\} \right\rangle P_n(\cos \phi) e^{i\omega t} \quad (\text{XII}) \end{aligned}$$

After separating the real and imaginary parts of Eq. (XII) in $\langle \rangle$, it can be written as

$$\begin{aligned}\sigma_{rr} = & \sum_{n=0}^{\infty} [\operatorname{Re}(a_n^*) + i\operatorname{Im}(a_n^*)](Q_1 + iQ_2)P_n(\cos\phi)e^{i\omega t} \\ & + \sum_{n=0}^{\infty} \frac{2\lambda_n}{r^2}(Q_3 + iQ_4)P_n(\cos\phi)e^{i\omega t}\end{aligned}\quad (\text{XIII})$$

where

$$\begin{aligned}Q_1 = & -q_1\operatorname{Re}[j_n(k, *r)] + q_2\operatorname{Im}[j_n(k, *r)] - 2(q_5q_{12} - q_6q_{13}) \\ & - \frac{4}{r} \left\{ q_3\operatorname{Re}[j_n'(k, *r)] - q_4\operatorname{Im}[j_n'(k, *r)] \right\}\end{aligned}$$

$$\begin{aligned}Q_2 = & q_1\operatorname{Im}[j_n(k, *r)] - q_2\operatorname{Re}[j_n(k, *r)] - 2(q_6q_{12} + q_5q_{13}) \\ & - \frac{4}{r} \left\{ q_3\operatorname{Im}[j_n'(k, *r)] + q_4\operatorname{Re}[j_n'(k, *r)] \right\}\end{aligned}$$

$$q_{12} = \left\{ [q_7 - \lambda_n\operatorname{Re}(k, *^2)]\operatorname{Re}[j_n(k, *r)] - \lambda_n\operatorname{Im}[j_n(k, *r)]\operatorname{Im}(k, *^2) \right\} / q_7$$

$$q_{13} = \left\{ [q_7 - \lambda_n\operatorname{Re}(k, *^2)]\operatorname{Im}[j_n(k, *r)] + \lambda_n\operatorname{Re}[j_n(k, *r)]\operatorname{Im}(k, *^2) \right\} / q_7$$

$$Q_3 = q_8 \left\{ \operatorname{Re}[j_n(k_2^*r)] - rq_{10} \right\} - q_9 \left\{ \operatorname{Im}[j_n(k_2^*r)] - rq_{11} \right\}$$

$$Q_4 = q_8 \left\{ \operatorname{Im}[j_n(k_2^*r)] - rq_{11} \right\} + q_9 \left\{ \operatorname{Re}[j_n(k_2^*r)] - rq_{10} \right\}$$

Finally, the normal stress can be expressed as

$$\sigma_{rr}(r, \phi, t) = \sum_{n=0}^{\infty} [Z_{n1}(r) + iZ_{n2}(r)]P_n(\cos\phi)e^{i\omega t}\quad (\text{XIV})$$

where

$$Z_{n1} = \operatorname{Re}(a_n^*) \cdot Q_1 - \operatorname{Im}(a_n^*)Q_2 + 2\lambda_n Q_3 / r^2$$

$$Z_{n2} = \operatorname{Re}(a_n^*) \cdot Q_2 + \operatorname{Im}(a_n^*)Q_1 + 2\lambda_n Q_4 / r^2$$

Eq. (XIV) is the desired expression to be shown.

NOMENCLATURE

E	Modulus of elasticity
E^*	Complex modulus of elasticity, $E' + iE''$
E', E''	Real and imaginary parts of E^* respectively
F_r	Radial force
G^*	Complex shear modulus, $G' + iG''$
G', G''	Real and imaginary parts of G^* respectively
$P_n(\cos\phi)$	Legendre polynomials of the first kind
$P_n'(\cos\phi)$	Associated Legendre polynomials of the first kind and first order
ϕ_n	Coefficients of the Legendre polynomial expansion of ϕ
ψ_n	Coefficients of the Legendre polynomial expansion of ψ
a	Radius of sphere
a_n, b_n	Coefficients of ϕ_n and ψ_n respectively
c_n	Coefficients of the Legendre polynomial expansion of locally applied radial displacement
$j_n(z)$	Spherical Bessel functions, $(\pi/2z)^{1/2} J_{n+1/2}(z)$
k_1, k_2	Wave numbers for the dilatational and shear waves respectively
k_1^*, k_2^*	Complex wave numbers for the dilatational and shear waves respectively
r, θ, ϕ	Spherical coordinates
t	Time
\bar{u}	Displacement vector
u, v, w	Components of the displacement vector in spherical coordinates
$\epsilon_{ij}, \sigma_{ij}$	Strain and stress tensors respectively
λ	Lamé first constant, $G(E-2G)/(3G-E)$
λ_n	$= n(n+1)$, where n are integers
ρ	Mass density

ω	Circular frequency
Δ	Cubical dilatation, $\frac{\partial w}{\partial r} + \frac{2w}{r} + \frac{1}{r} \frac{\partial u}{\partial \phi} + \frac{\cot \phi}{r} u$
∇	Gradient operator
$\nabla \times$	Curl operator

Note that every quantity which has superscript star is a complex number or function.

LIST OF FIGURES

Fig. 1 Model for theoretical analysis

Fig. 2 Spherical coordinate system

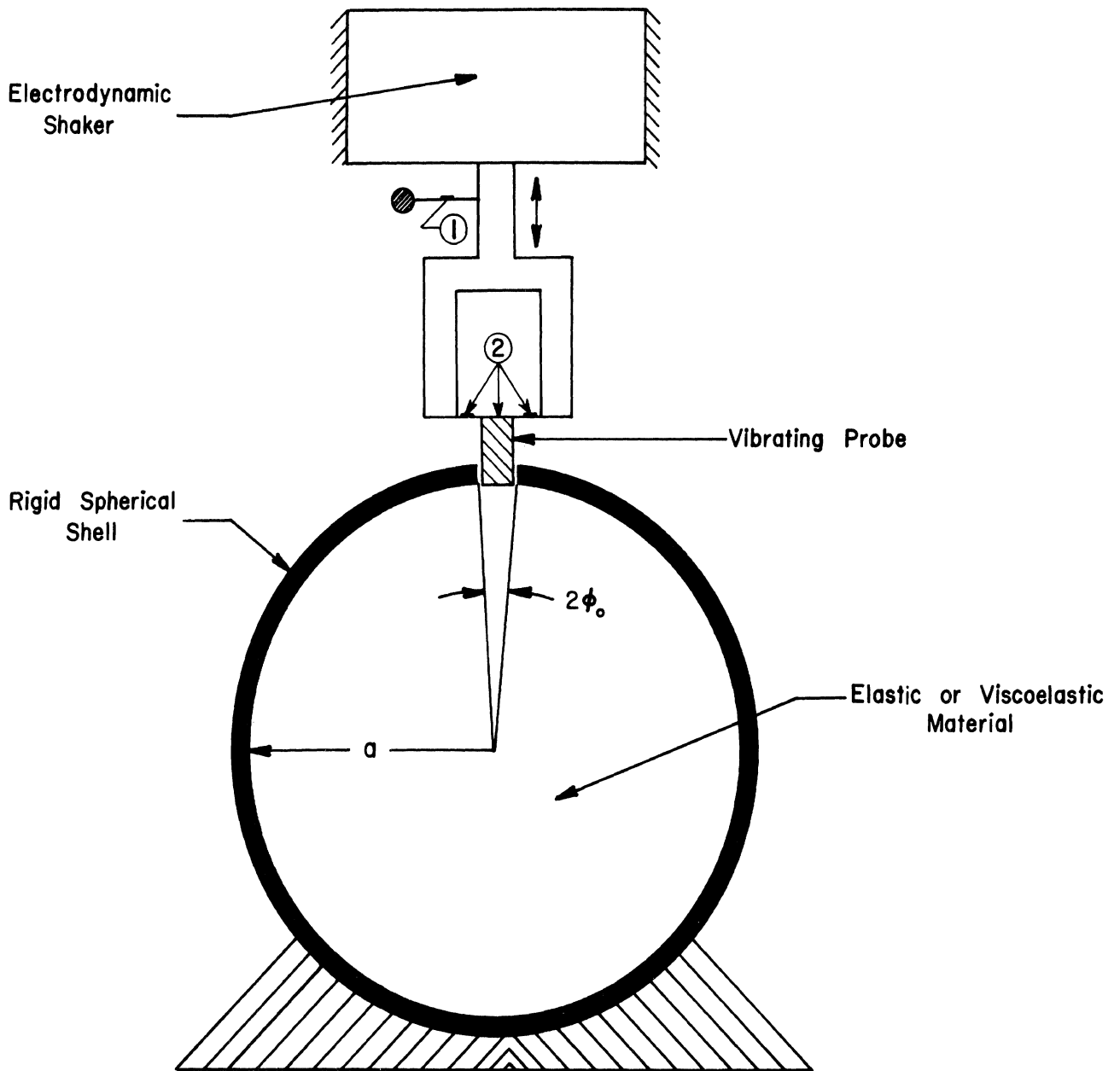


Fig. 1. MODEL for THEORETICAL ANALYSIS

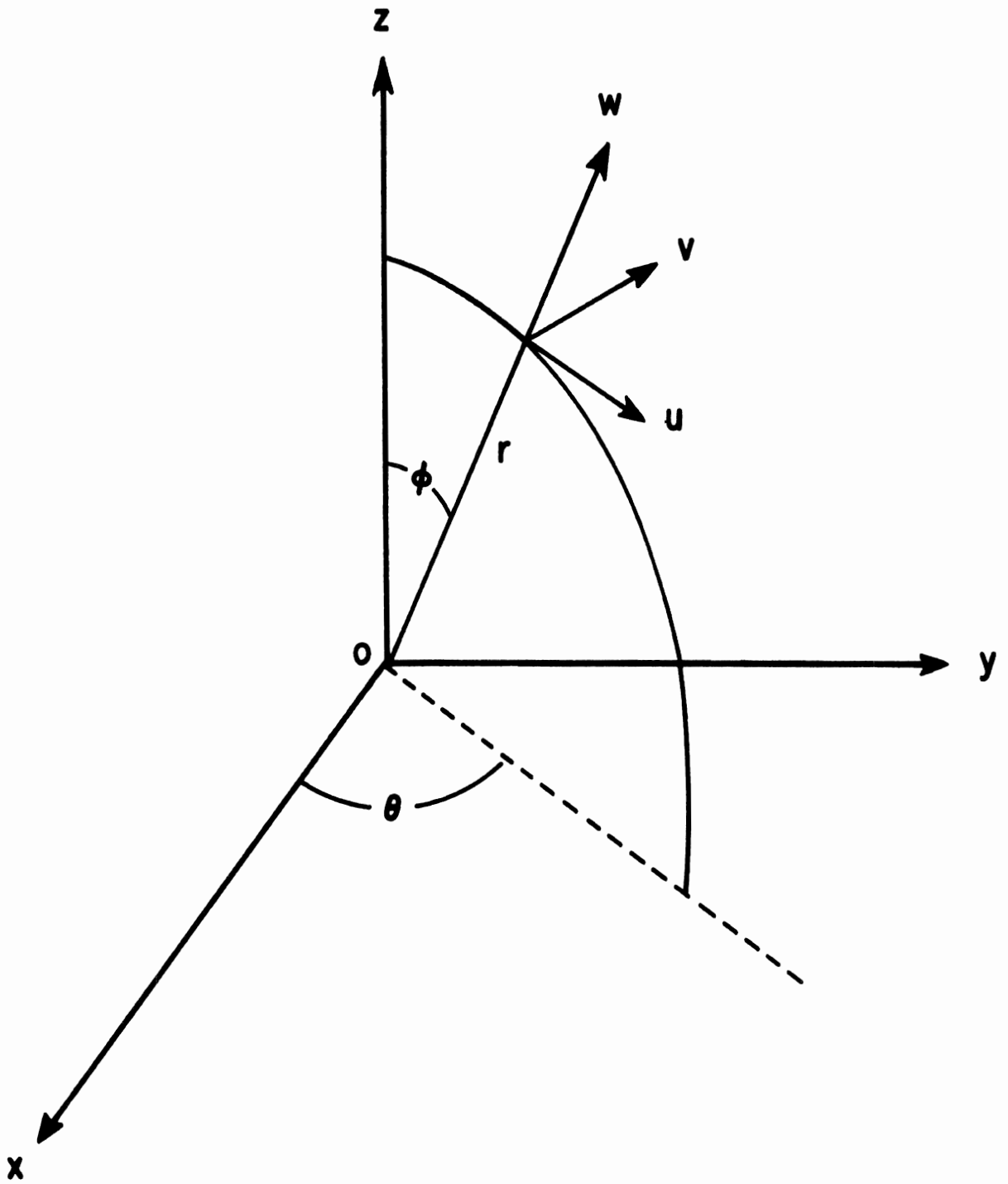


Fig. 2. SPHERICAL COORDINATE SYSTEM

